# Gravitational waves from coalescing binaries and Doppler experiments

Bruno Bertotti
*Dipartimento di Fisica Nucleare e Teorica, Università di Pavia, 27100 Pavia, Italy*

Alberto Vecchio
*Max Planck Institut für Gravitationsphysik, Albert Einstein Institut, 14473 Potsdam, Germany*

Luciano Iess
*Dipartimento Aerospaziale, Università ''La Sapienza,'' 00158 Roma, Italy*
(Received 21 April 1998; published 1 March 1999)

Doppler tracking of interplanetary spacecraft provides the only method presently available for broadband searches of low frequency gravitational waves ($\sim 10^{-5}$–1 Hz). The instruments have a peak sensitivity around the reciprocal of the round-trip light time $T$ ($\sim 10^3$–$10^4$ sec) of the radio link connecting Earth to the space probe and therefore are particularly suitable to search for coalescing binaries containing massive black holes in galactic nuclei. A number of Doppler experiments—the most recent involving the probes ULYSSES, GALILEO, and the Mars Observer—have been carried out so far; moreover, in 2001–2004 the CASSINI spacecraft will perform three 40-day data acquisition runs with an expected sensitivity about 20 times better than that achieved so far. The central aims of this paper are (i) to explore, as a function of the relevant instrumental and astrophysical parameters, the Doppler output produced by *inspiral* signals—sinusoids of increasing frequency and amplitude (the so-called *chirp*), (ii) to identify the most important parameter regions where to concentrate intense and dedicated data analysis, and (iii) to analyze the all-sky and all-frequency sensitivity of the CASSINI experiments, with particular emphasis on possible astrophysical targets, such as our galactic center and the Virgo cluster. We consider first an ideal situation in which the spectrum of the noise is white and there are no cutoffs in the instrumental band; we can define an *ideal* signal-to-noise ratio (SNR) which depends in a simple way on the fundamental parameters of the source—*chirp mass* $\mathcal{M}$ and luminosity distance—and the experiment—round-trip light time and noise spectral level. For any *real* experiment we define the *sensitivity function* $\Upsilon$ as the degradation of the SNR with respect to its ideal value due to a colored spectrum, the experiment finite duration $T_1$, the accessible frequency band $(f_b, f_e)$ of the signal, and the source's location in the sky. We show that the actual value of $\Upsilon$ crucially depends on the overlap of the band $(f_b, f_e)$ with the instrument response: the sensitivity is best when $f_b \lesssim 1/T$ and $f_e$ coincides with the frequency corresponding to the beginning of the merging phase. Furthermore, for any $f_b$ and $T_1$, there is an optimal value of the chirp mass—the *critical chirp mass* $\mathcal{M}_c \propto f_b^{-8/5} T_1^{-3/5}$—that produces the largest sensitivity function; lower values of $\mathcal{M}$ correspond to a smaller bandwidth and lower SNR. Also the optimal source's location in the sky strongly depends on $(f_b, f_e)$. We show that the largest distance at which a source is detectable with CASSINI experiments is $\sim 600$ Mpc and is attained for massive black holes of comparable masses $\sim 10^7 M_\odot$ and $f_b \sim 10^{-5}$ Hz. Sources not far from coalescence in the Virgo cluster with $10^6 M_\odot \lesssim \mathcal{M} \lesssim 10^9 M_\odot$ would be detectable with a SNR $\sim 1$–30. The SNR and the range of accessible masses reduce drastically when a smaller mass ratio is considered. We then turn our attention to galactic observations, in particular on the detectability of a coalescing binary in the galactic center, where a small black hole of mass $M_2$ could be orbiting around the central massive one $M_1 \simeq 2 \times 10^6 M_\odot$. CASSINI would be able to pick up such systems with $M_2 \gtrsim 50 M_\odot$; for $M_2 \gtrsim 10^3 M_\odot$ the SNR could be as high as $\sim 100$–1000. It may also be possible to detect such binaries in more than one of the three CASSINI experiments, thus reenforcing the confidence of detection.
[S0556-2821(99)04602-0]

PACS number(s): 04.80.Nn, 97.60.Lf, 98.62.Js

## I. INTRODUCTION

The search for gravitational waves has grown greatly in the last few years: four ground-based laser interferometers—the Laser Interferometric Gravitational Wave Observatory (LIGO) [1], VIRGO [2], GEO600 [3], and TAMA [4]—with optimal sensitivity in the band $\sim 10$ Hz–1 kHz are now under construction and are scheduled to be in operation by the turn of the century; at the same time, the sensitivity of acoustic narrow-band devices in the kHz regime is steadily improving [5–9]. In this high frequency band the most interesting sources are connected to collapsed objects with a mass in the range $\sim 1 M_\odot - 1000 M_\odot$. However, at low frequencies (below a few Hz) detectors on Earth are severely impaired by seismic noise. To observe sources of higher mass one must use instruments in space, sensitive in the mHz band.

The Doppler tracking of interplanetary spacecraft [10] is the only method presently available to search for gravitational waves in the low frequency regime ($\sim 10^{-5}$–1 Hz). Several experiments have been carried out so far, all of them with *nondedicated* space probes: Voyager 1 [11], Pioneer 10 and 11 [12,13], ULYSSES [14,15], GALILEO, and the Mars

 

TABLE I. Summary of Doppler experiments to search for gravitational waves. $T_1$ is the effective length of data available, $\sigma_y$ the average effective Allan variance of the data, and $T$ the average round-trip light time of the radio link during the data acquisition runs. The frequency bands of the up-link ($S$, 2.1 GHz; $X$, 7.2 GHz; $K_a$, 32 GHz) and down-link ($S$, 2.3 GHz; $X$, 8.4 GHz; $K_a$, 34 GHz) carriers are shown in the two final columns. For the four short experiments carried out with Pioneer 10 and 11 and Voyager 1 see [21] and references therein.

| Space probe | $T_1$/days | $\sigma_y$ | $T$/sec | Up-link | Down-link |
|---|---|---|---|---|---|
| ULYSSES 3 Dec. 90–4 Jan. 91 | 3.5 | $3\times10^{-14}$ | 600 | $S$ | $S,X$ |
| ULYSSES 20 Feb. 92–18 Mar. 92 | 14 | $7\times10^{-14}$ | 4430 | $S$ | $S,X$ |
| ULYSSES Mar. 93–Apr. 93 | 19 | $1.4\times10^{-13}$ | 4100 | $S$ | $S,X$ |
| GALILEO Mar. 93–Apr. 93 | 19 | $2.3\times10^{-13}$ | 945 | $S$ | $S$ |
| Mars Observer Mar. 93–Apr. 93 | 19 | $5\times10^{-14}$ | 1150 | $X$ | $X$ |
| CASSINI 26 Nov. 01–5 Jan. 02 | 40 | $3\times10^{-15}$ | 5783 | $X,K_a$ | $X,K_a$ |
| CASSINI 7 Dec. 02–16 Jan. 03 | 40 | $3\times10^{-15}$ | 7036 | $X,K_a$ | $X,K_a$ |
| CASSINI 15 Dec. 03–24 Jan. 04 | 40 | $3\times10^{-15}$ | 7859 | $X,K_a$ | $X,K_a$ |

Observer [16]. They suffer from the limitations of instrumentation designed for other purposes and from several disturbances, including those due to the ground sector; however, their sensitivity is astrophysically interesting, even though the rate of detectable events is uncertain and (probably) low, given the current instrument performances. At present a large amount of data is available: a major experiment lasting 28 days was carried out with ULYSSES in February and March 1992 [15] and a 20-day coincidence experiment was performed in the Spring 1993 with the spacecraft GALILEO, Mars Observer, and ULYSSES [16] (see Table I).

The space probe CASSINI—a NASA-ESA-ASI joint mission [17]—represents the next step in Doppler experiments. It was launched on 15 October 1997 with the primary target being the study of the Saturn system, in particular its satellite Titan: at the first flyby with Titan, the Huygens probe will be released and descend into its atmosphere for a thorough investigation. CASSINI carries on board much improved instrumentation and will perform three long (40 days each) data acquisition runs in 2001–2004 to search for gravitational waves [18] with expected sensitivity about 20 times better than that achieved so far; indeed this mission offers the most promising opportunity to date to search for low frequency signals. The target planet Saturn will be reached on 1 July 2004, after a long cruise phase which includes two Venus, one Earth and one Jupiter flyby. This complex trajectory provides the heavy spacecraft (5650 kg, over half of which is propellant for several orbital maneuvers) with an additional 6 km/s velocity increment needed to reach Saturn. The long cruise phase provides three opportunities for gravitational wave observations, about the solar oppositions in December 2001, December 2002, and January 2004, when the spacecraft is beyond Jupiter's orbit, at geocentric distances of 6.7, 8.0, and 8.8 AU. These periods have been chosen in order to reduce the effects of interplanetary plasma on the radio link, which are indeed minimum when the Earth-spacecraft line of sight is approximately parallel to the solar wind velocity. In the cruise phase the on-board activity is minimal and the spacecraft is therefore in a very stable dynamical and thermal state, thus in the best conditions for the measurements. Making experiments at large heliocentric distances not only allows the coverage of a large spectral window but also gives the spacecraft a good immunity to nongravitational accelerations, whose effects are further reduced by the small area-to-mass ratio (about $2.1\times10^{-3}$ $m^2/kg$).

The next, far away, and much more ambitious projects to search for low frequency gravitational wave radiation will probably involve interferometers in space with arms of $10^6$'s of km [19,20] (see also [21] and references therein for a review of detectors in space).

In the low frequency band we expect five main types of sources (for an extensive discussion regarding the whole gravitational wave spectrum we refer the reader to [22,23]):

(1) Catastrophic, wideband collapses of large masses, possibly in dense concentrations of matter and stars, leading to the formation of a massive black hole (MBH); the search for such signals motivated the original proposal of Doppler experiments [24].

(2) Short-period binary systems of solar mass compact objects [25–27]; among them the binary pulsar PSR 1913+16 [28,29], whose study over the past 25 years has provided the most clear *indirect evidence* of the existence of gravitational waves [30]; however, stellar mass binaries are not detectable with present and near-future Doppler experiments, due to inadequate sensitivity and short duration.

(3) Solar mass compact objects orbiting a massive black hole in galactic cores [31–33].

(4) Binary systems of massive black holes spiraling together toward their final coalescence [34–36].

(5) Backgrounds of gravitational waves of primordial origin or generated by the superposition of radiation coming from unresolved binaries [37–41].

Here we will consider signals emitted by binary systems containing massive black holes, therefore sources at points 3 and 4, and the main goals of the paper are the exploration of

the structure of the Doppler output produced by inspiral signals from coalescing binaries and the analysis of the all-sky and all-frequency sensitivity of Doppler experiments with emphasis on the CASSINI mission.

Compelling arguments suggest the presence of MBH's in the nuclei of most galaxies, as the near-inevitable by-product of the infall of gas in their potential well [42–44] and MBH's are invoked to explain a number of phenomena, such as the activity of quasars and active galactic nuclei [45–48]. However, the observational evidence of their existence comes mainly from observations of relatively nearby galaxies, whose nuclei do not show significant activity. Central dark masses—which are believed to be ''dead quasars'' [49]—are mainly inferred by studying the spatial distribution and velocity of gas and/or stars in galactic cores. About ten candidate massive black holes, with mass in the range $\sim 10^6 M_\odot - 10^9 M_\odot$, are known today and we refer the reader to [50–53] for recent reviews. The most striking evidence comes from the mapping of the gas motion via the 1.35 cm water maser emission line in NGC 4258 and the observations in the near-infrared band of the star motion in our galactic center. In the case of NGC 4258, observations with the Very Long Baseline Array have allowed to measure the velocity of the gas in the disk with an accuracy of 1 km/sec: the disk rotates with a velocity exactly in agreement with the Kepler law, due to the presence of an obscure object of mass $\simeq 3.6\times 10^6 M_\odot$ [54]. Regarding our galactic center, recent observations with the New Technology Telescope of the proper motion of stars in the core have shown that their speed scales as the inverse of the square root of the distance from the center up to 20 000 km/sec; the inferred mass of the dark body is $\simeq 2.5\times 10^6 M_\odot$ [55]. In both cases only exotic (and highly implausible) alternatives to a MBH can still be considered [56,57].

Many galaxies have experienced at least a merger since the epoch $z>2$ [58,59]. If a MBH is present in each core of both interacting galaxies, the two massive objects would fall into the common potential well, forming a pair which loses energy and angular momentum through dynamical friction; eventually a binary forms and, driven by radiation reaction, progresses toward the final coalescence. This scenario provides, therefore, quite a natural way of producing massive binary black holes (MBHB's) [34]. The apparent precession and bending of jets in active galaxies [34,60] and Doppler-shifted broad emission line peaks in quasars [61] are possible indirect evidence of the existence of such systems. Moreover, observations of MBHB's in the nuclei 1928+738 [62], OJ287 [63,64], and 3C 390.3 [65] have been claimed.

MBH's in the center of galaxies are surrounded by a dense cluster of ordinary stars, whose tidal disruption provides the gas to refuel the central object, white dwarfs, neutron stars, and low mass back holes, probably in the mass range $\sim 5M_\odot - 100M_\odot$. Contrary to ordinary stars, compact objects are not disrupted by the hole and can occasionally be captured, presumably on highly eccentric orbits, forming binary systems with life shorter than the Hubble time. Moreover, the orbits of objects with mass $\gtrsim 5M_\odot$ around the central massive body would not be perturbed by other stars in the core, providing therefore clean gravitational wave signals, which can be used to extract valuable information about the central object [66,67].

From the data analysis point of view, where the structure of the signal determines the choice of the optimal detection algorithm, it is convenient to divide the entire process of binary *coalescence* into three separate phases.

(a) *Adiabatic inspiral*: the bodies are driven by radiation reaction from their initial distance to smaller separations, losing energy and angular momentum. The emitted gravitational wave is a sinusoid of increasing frequency and amplitude (the so-called *chirp*). In this paper we will make two important assumptions: (i) when the signal enters the sensitivity window of the detector, the orbit has already been circularized; in fact, the eccentricity $e$ diminishes with the frequency $f$ according to $e^2(t)\propto f^{-19/9}(t)$ [68]. Even a binary born with $e\sim 1$ and a period of 100 yr, say, would carry a residual eccentricity $\lesssim 10^{-4}$ when the signal can be picked up by the instrument. For binaries composed of two MBH's that have undergone a common evolution inside a galactic core, this assumption is reasonable, even though a full understanding of massive binary evolution before radiation reaction takes over is still lacking [69–71]. The condition $e \ll 1$ is likely to be violated for solar mass compact objects orbiting a massive one in a highly elliptic orbit, which may maintain a non-negligible eccentricity throughout the inspiral [31]. This would bring about a different scenario, with shorter lifetime and emission of gravitational waves at multiples of the orbital frequency [72]. (ii) In modeling the waveform we will use the lowest-order Newtonian quadrupolar approximation, as we are mainly aiming at the estimation of the signal-to-noise ratio (SNR) and not at the construction of signal templates for matching filters [73,74].

(b) *Merger*: when the body separation $r$ reaches a value of about $6M$, where $M$ is the source's total mass, the orbit becomes unstable and the binary begins the final deadly phase of plunge-in. The signal consists in a wideband burst of duration $\sim M$, but the details of the emitted radiation are in large part still unknown.

(c) *Ring-down*: the single black hole formed during the merging phase settles down oscillating according to quasi-normal modes. The emitted waves consist of a superposition of exponentially damped sinusoids.

In this paper we will concentrate on radiation emitted during the inspiral phase. Such signals can be usefully classified according to the best algorithm to extract them in a given data set [15].

(I) *Periodic signals*: the rate of change of the frequency is too small to be detected with the instrumental frequency resolution. Here the ordinary techniques for the search of periodic oscillations of unknown frequency apply.

(II) *Linearly ''chirped'' signals*: the frequency drift is larger than the frequency resolution of the detector, but the change in frequency due to its second time derivative during the observation time can be neglected, so that we can assume a linear increase of $f(t)$ with a constant rate $\beta = df/dt$. An efficient technique to search for these signals has been developed in [75–77] and already applied to several data sets [15]; for every allowed $\beta$, the chirping signal is reduced to a periodic one and standard methods can be applied.

These two classes correspond to sources which are far from coalescence—in fact $df(t)/dt \propto f^{-8/3}(t)$ [see Eq. (2.2)]—and, for a given distance, weaker; therefore, the search depth (the maximum distance at which a binary would be detectable) is very limited: in [15] we showed that, with signals of this class, the galactic center is marginally accessible with the best data available today.

(III) *General chirps*: the assumed signal has the correct evolution in frequency, but the merger does not occur inside the record.

(IV) *Chirps and bursts*: the record contains the final part of the chirping waveform and the wideband burst produced just before the engulfment of one black hole into the horizon of the other.

These classes of signals can be distinguished in the record by the frequency and its change; for a given frequency, its drift increases with the class. Roughly speaking, this ordering corresponds to stronger sources and, therefore, to larger attainable distances.

Although in the final phase of the inspiral the two bodies have high velocities ($v/c > 0.1$) and the description of their gravitational wave emission requires a relativistic approach [22], we shall use the quadrupole Newtonian approximation for the estimation of the SNR. The use of this approximation has the advantage that the inspiral signal depends on only *one physical parameter*, the *chirp mass* $\mathcal{M}$; see Eq. (2.3). In principle it can be derived from the measurement of the frequency $f$ and its rate of change $df/dt$; then the amplitude $A \propto \mathcal{M}^{5/3} f^{2/3}/D$ provides the distance $D$ of the source. We can therefore determine, for any given experiment, the largest attainable distance; we call it, for a given class, the *ken* of the experiment. This is another example, similar to the one pointed out by Schutz in [78], of the power of gravitational wave astronomy when a simple source model is available. The central aim of this paper is to fully develop the richness of these concepts when applied to Doppler experiments and to link possible astrophysical sources (like those in the Virgo cluster and/or in the galactic center) to the actual data. In particular we will apply the main results to the set of experiments scheduled during the CASSINI mission.

Doppler tracking of interplanetary spacecraft provides a wideband detector of gravitational waves in the low frequency regime (but it can also be used as a narrow-band xylophone instrument [79]). A very stable electromagnetic signal in the GHz radio band is continuously transmitted from Earth to the spacecraft and coherently transponded back in order to monitor the change of their relative velocity. The optimal sensitivity of the detector is at frequencies of the order of the inverse of the round-trip light time $T$ of the Earth-spacecraft radio link. However, since in practice the duration of the experiment is not large, only a limited frequency interval of a chirping signal is accessible. There are two modes of search for a signal: if the frequency interval is small, *narrow-band search*, one looks for sources far from the final plunge-in, hence at a small distance. In a *wideband search* the signal is stronger and one can detect radiation emitted by binary systems farther away. In the past, the analysis of Doppler data has been confined mainly to the narrow-band case (classes I and II); in this paper we concentrate on the more interesting wideband case and aim at sources at larger distances, but detectable only for a smaller fraction of their lifetime. The largest ''ken'' is, of course, attained for class IV, which merges into the class of generic, wideband bursts. The search for bursts in the records of the 1993 GALILEO–Mars Observer–ULYSSES coincidence experiment is currently in progress [16]. However this analysis must be a rough one, as the structure of the signal in this strongly relativistic regime is essentially unknown and the use of data collected in coincidence by several instruments is crucial.

The paper is organized as follows. In Sec. II we review the basic concepts and formula (partially to fix notation) regarding the gravitational wave emission from binaries. In Sec. III we introduce the signal $y(t)$ produced at the output of a Doppler detector by a gravitational wave train $h(t)$: in Fourier space, $\tilde{y}(f)$ is the product of $\tilde{h}(f)$ and the Doppler *three-pulse response function* $\tilde{r}_\theta(f)$; we review the main properties of $\tilde{r}_\theta(f)$ and in particular stress its different structure at low ($f \lesssim 1/T$) and high ($f \gtrsim 1/T$) frequencies. Section IV contains the main results of the paper: a thorough analysis of the signal-to-noise ratio produced by inspiral signals in Doppler experiments as a function of the parameters that characterize the source and the instrument: the chirp mass $\mathcal{M}$ (and the mass ratio), the instantaneous emission frequency of the signal $f_b$ when the instrument is ''turned on,'' the duration of the observation $T_1$, the structure of the instrument noise spectral density $S_n(f)$, the location $\theta$ of the source in the sky with respect to the detector arm, and the round-trip light time $T$. This analysis is carried out in full generality and can be applied to any Doppler experiment. We define the *ideal* SNR $\rho_{\rm id}$ as that corresponding to unlimited bandwidth, $\theta = \pi/2$, and flat noise spectrum: $\rho_{\rm id}$ depends only on $\mathcal{M}$, $T$, $D$, and the noise spectral level $S_0$. Of course, in a real experiment several factors—including the finite observation time, the signal bandwidth, the frequency-dependent noise spectral density, and the position of the source in the sky—contribute to degrade the SNR. We define the *sensitivity function* $\Upsilon$ as the actual SNR with respect to its ideal value. $\Upsilon$ is extensively studied in Sec. IV A; in particular we show that the maximum value of $\Upsilon$ is achieved when $0.1/T \lesssim f_b \lesssim 1/T$ and the binary chirp mass is close to what we call its critical value $\mathcal{M}_c \propto T_1^{-3/5} f_b^{-8/5}$. In Sec. IV B we study CASSINI's sensitivity (and compare it with that of ULYSSES), with emphasis on possible sources in the Virgo cluster and the galactic center. We show that the maximum reachable distance is $\sim 600$ Mpc; binaries close to the final coalescence with $10^6 M_\odot \lesssim \mathcal{M} \lesssim 10^9 M_\odot$ and comparable masses would be detectable in the Virgo cluster with SNR up to 30; in galactic searches, CASSINI would be able to pick up (possibly in all three data sets) signals from the inspiral of a secondary black hole of mass $M_2 \gtrsim 50 M_\odot$ onto the central one, $M_1 \simeq 2 \times 10^6 M_\odot$. Finally, Sec. V contains a discussion about the probability of success of Doppler experiments based on simple conventional astrophysical scenarios and our conclusions.

We take units in which $c = G = 1$, so that velocities are dimensionless and $10^6 M_\odot \simeq 4.926$ sec.

## II. EXPECTED SIGNAL

### A. Chirped precursor

We consider a binary system of two compact objects of mass $M_1$ and $M_2$; $M \equiv M_1 + M_2$ and $\mu \equiv M_1 M_2 / M$ are the total and reduced mass, respectively; the orbital parameters evolve secularly due to the loss of energy and angular momentum by emission of gravitational waves.

We shall assume that, when the gravitational signal enters the sensitivity window of the detector, the radiation reaction has already circularized the orbit. Under this assumption, in the Newtonian quadrupolar approximation, the frequency $f$ of the emitted gravitational wave is twice the orbital frequency of the binary, namely,

$$f^2(t) = \frac{M}{\pi^2 r^3(t)}, \tag{2.1}$$

where $r(t)$ is the orbital separation. In the Newtonian model, $f(t)$ evolves according to [80]

$$\dot{f}(t) = \frac{96}{5} \pi^{8/3} \mathcal{M}^{5/3} f^{11/3}(t), \tag{2.2}$$

where the overdot indicates the time derivative and

$$\mathcal{M} \equiv \mu^{3/5} M^{2/5} = \eta^{3/5} M \quad \left( \eta \equiv \frac{\mu}{M} \leqslant \frac{1}{4} \right) \tag{2.3}$$

is the so-called *chirp mass*; in this approximation $\mathcal{M}$ is the only *dynamical* parameter that regulates the evolution of the frequency and the amplitude of the wave.

Let us consider a signal emitted by a binary at a luminosity distance $D$ and let $\iota$ be the angle between the wave propagation direction and the orbital angular momentum $\boldsymbol{L}$. The strain at the detector reads

$$\begin{aligned} h(t) &= h_+(t) \cos 2\varphi + h_\times(t) \sin 2\varphi \\ &= A(t) \cos\left[ 2\pi \int^t dt' f(t') + \varphi_0 \right], \end{aligned} \tag{2.4}$$

where $h_+(t)$ and $h_\times(t)$ are the two independent polarization states [90], $\varphi$ is a polarization angle,

$$\begin{aligned} A(t) &= 2\, Q(\iota, \varphi) \frac{\mathcal{M}^{5/3}}{D} [\pi f(t)]^{2/3} = 1.3 \times 10^{-15}\, Q(\iota, \varphi) \\ &\times \left( \frac{D}{\mathrm{Mpc}} \right)^{-1} \left( \frac{f}{10^{-4}\ \mathrm{Hz}} \right)^{2/3} \left( \frac{\mathcal{M}}{10^6 M_\odot} \right)^{5/3} \end{aligned} \tag{2.5}$$

is the amplitude of the signal, and

$$\varphi_0 = \tan^{-1}\left[ \frac{2 \cos\iota \sin(2\varphi)}{\cos(2\varphi)(1 + \cos^2\iota)} \right] \tag{2.6}$$

gives the polarization phase. The quantity

$$Q^2(\iota, \varphi) = [\cos^2(2\varphi)(1 + \cos^2\iota)^2 + 4 \cos^2\iota \sin^2(2\varphi)] \tag{2.7}$$

depends on the orientation of the binary and, for random values, $\langle Q^2 \rangle = 8/5$, where $\langle\ \rangle$ stands for the average with respect to $\iota$ and $\varphi$: $Q(\iota, \varphi)$ ranges from 0 (for $\iota = \pi/2$, $\varphi = \pi/4$) to 2 (for $\iota = 0$ or $\pi$) [91].

Integrating Eq. (2.2), it is straightforward to derive the frequency evolution of the wave,

$$f(t) = \frac{1}{8\pi} \left( \frac{5}{t_n} \right)^{3/8} \mathcal{M}^{-5/8} \left( 1 - \frac{t}{t_n} \right)^{-3/8}, \tag{2.8}$$

and therefore the phase of the gravitational signal reads

$$\Phi(t) = 2\pi \int_t^{t_n} dt' f(t') = \Phi_n - 2 \left( \frac{t_n - t}{5\mathcal{M}} \right)^{5/8}; \tag{2.9}$$

equivalently,

$$t(f) = t_n - 5 (8\pi f)^{-8/3} \mathcal{M}^{-5/3}, \tag{2.10}$$

$$\Phi(f) = \Phi_n - 2 (8\pi \mathcal{M} f)^{-5/3}. \tag{2.11}$$

From Eq. (2.2), one can also derive the number of Newtonian wave cycles spent by a binary while it sweeps the relevant frequency interval:

$$\mathcal{N}(f) = \int_f^\infty \frac{f'}{\dot{f}'} df' = \mathcal{N}_n - \frac{1}{\pi} (8\, \pi \mathcal{M} f)^{-5/3}. \tag{2.12}$$

$t_n$, $\Phi_n$, and $\mathcal{N}_n$ are integration constants, defined as the values that $t(f)$, $\Phi(f)$, and $\mathcal{N}(f)$ formally take when $f = \infty$ $(r = 0)$. Of course, the signal must be cut off when the inspiral phase ends and the merger begins. The fully relativistic two-body problem is still unsolved; it is mainly investigated using post-Newtonian approximations (see [81,82] and references therein) and numerical techniques (see [94–96] and references therein). For simplicity we will neglect the radiation coming from frequencies higher than

$$f_{\mathrm{isco}} = \frac{1}{6^{3/2}\, \pi M} \simeq 1.9 \times 10^{-3}\, (4\eta)^{3/5} \left( \frac{\mathcal{M}}{10^6\, M_\odot} \right)^{-1} \mathrm{Hz}, \tag{2.13}$$

corresponding to the *innermost stable circular orbit* $r_{\mathrm{isco}} = 6\, M$ for a test mass in the Schwarzschild field of a mass $M$. For $r < r_{\mathrm{isco}}$ (and velocity larger than $v_{\mathrm{isco}} \simeq 0.408$) orbits are unstable. For general black holes and mass ratios we can write $r_{\mathrm{isco}} = 6\, k\, M$, with $k \approx 1$ (several methods have been used to estimate the exact value of $k$, but a satisfactory answer is still lacking; see [97–100] for further details). In the Newtonian approximation we assume that $f_{\mathrm{isco}} = f(t_c)$ separates, at the time $t_c$, the inspiral phase from the broadband plunge-in. The major feature of the relativistic corrections is, therefore, to *anticipate* the final plunge.

If an experiment takes place in the time interval from $t = 0$ to $t = T_1$, we define

$$f_b \equiv f(t = 0) \tag{2.14}$$

as the frequency at which the signal enters the record at $t=0$; the frequency at the end, after the observation time $T_1$, is

$$f_e \equiv f(t=T_1) = \min\left[ f_b\left(1-\frac{T_1}{t_n}\right)^{-3/8}, f_{\rm isco}\right]. \quad (2.15)$$

If $f_b(1-T_1/t_n)^{-3/8} > f_{\rm isco}$, the record includes the merger signal and is of class IV; otherwise we have class III signals. The Newtonian time to coalescence for a system radiating at frequency $f_b$ at the beginning of the record is given by

$$\tau_n = 5\,(8\pi f_b)^{-8/3}\,\mathcal{M}^{-5/3}. \quad (2.16)$$

It is also useful to note that the time for a signal to sweep from the frequency $f_b$ to the beginning of the final coalescence at $f=f_{\rm isco}$ is

$$\tau_c = 5\,(8\pi)^{-8/3}\,\mathcal{M}^{-5/3}(f_b^{-8/3} - f_{\rm isco}^{-8/3}). \quad (2.17)$$

We define

$$f_B \equiv f_{\rm isco}\left(1+\frac{T_1}{5(8\pi f_{\rm isco})^{-8/3}\,\mathcal{M}^{-5/3}}\right)^{-3/8} \quad (2.18)$$

as the initial frequency of a gravitational wave whose final frequency is $f_{\rm isco}$; it depends on $\mathcal{M}$, $\eta$, and $T_1$ and corresponds to the largest initial frequency that produces class III signals.

On the basis of the model of the waveform we can now formalize the distinction of the signals in classes that we introduced in Sec. I. Being based upon the actual record, it is particularly useful for data analysis. It refers to the frequency resolution $1/T_1$ of the experiment and will allow us to divide the two-dimensional parameter space $(\mathcal{M}, f_b)$, where the inspiral signal is defined, into a *periodic region*, a *linear region*, and a *general chirp region* (of class III and IV, depending whether the final burst is within the record or not). This distinction is justified by the great simplicity and low computational load of the data analysis when the frequency is constant (class I) or varies linearly with time (class II); these two cases are extensively discussed, and applied to the data of ULYSSES' second opposition, in [15]. When

$$T_1^2 \dot f(t) = \frac{96}{5}\pi^{8/3} T_1^2 \mathcal{M}^{5/3} f^{11/3} < 1 \quad \text{(class I)}, \quad (2.19)$$

we have periodic signals; when

$$T_1^3 \frac{\ddot f(t)}{2} = \frac{16896}{25}\pi^{16/3}\,T_1^3\,\mathcal{M}^{10/3} f^{19/3} < 1,$$

$$T_1^2 \dot f(t) > 1 \quad \text{(class II)}, \quad (2.20)$$

the frequency acceleration is negligible (''linear signals'');

$$\frac{T_1^3 \ddot f(t)}{2} > 1, \quad \text{and } f_b < f_{\rm isco} \text{ (class III/IV)} \quad (2.21)$$

correspond to general chirps [101]. Referring to a chirp mass $\mathcal{M}$ and observation time $T_1$, the initial frequency $f_b$ that separates out the four regimes reads

$$f_b \simeq \begin{cases} 5.1\times10^{-5}\left(\dfrac{T_1}{10^6\ \rm sec}\right)^{-6/11}\left(\dfrac{\mathcal{M}}{10^6 M_\odot}\right)^{-5/11}\ \text{Hz} & \text{(I-II)}, \\ 5.4\times10^{-5}\left(\dfrac{T_1}{10^6\ \rm sec}\right)^{-9/19}\left(\dfrac{\mathcal{M}}{10^6 M_\odot}\right)^{-10/19}\ \text{Hz} & \text{(II-III)}, \\ 1.9\times10^{-3}\,(4\eta)^{3/5}\left(\dfrac{\mathcal{M}}{10^6\,M_\odot}\right)^{-1}\left[1+8.7\times10^2\,(4\eta)^{8/5}\left(\dfrac{T_1}{10^6\ \rm sec}\right)\left(\dfrac{\mathcal{M}}{10^6\,M_\odot}\right)^{-1}\right]^{-8/3}\ \text{Hz} & \text{(III-IV)}. \end{cases} \quad (2.22)$$

The partition of the plane $(\mathcal{M}, f_b)$ in classes for a single CASSINI experiment ($T_1 = 40$ days) is given in Fig. 1. The values of $\tau_n$ that correspond to the transition between two adjacent classes read

$$\tau_n \simeq \begin{cases} 6.1\times10^7\left(\dfrac{\mathcal{M}}{10^6\,M_\odot}\right)^{-5/11}\left(\dfrac{T_1}{10^6\ \rm sec}\right)^{16/11}\ \text{sec} & \text{(I-II)}, \\ 2.6\times10^6\left(\dfrac{\mathcal{M}}{10^6\,M_\odot}\right)^{-5/19}\left(\dfrac{T_1}{10^6\ \rm sec}\right)^{24/19}\ \text{sec} & \text{(II-III)}, \\ 1.1\times10^3\left(\dfrac{\eta}{1/4}\right)^{-8/5}\left(\dfrac{\mathcal{M}}{10^6\,M_\odot}\right)\ \text{sec} & \text{(III-IV)}. \end{cases} \quad (2.23)$$

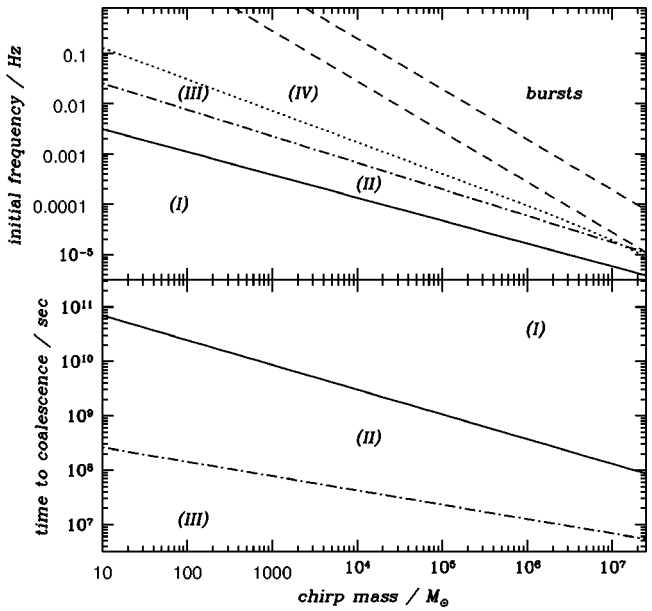


FIG. 1. Classes of coalescing binary signals for one of the three CASSINI experiments ($T_1=40$ days). The upper panel shows the partition of the plane $(\mathcal{M},f_b)$ in periodic (I), linear (II), and nonlinear regions. The dotted line divides nonlinear chirps in signals of class III and IV. The dashed lines indicate the boundary between signals of class IV and bursts—i.e., $f_{\rm isco}$ as a function of $\mathcal{M}$—for $M_2/M_1=0.01$ (lower line) and 1 (upper line). The lower panel shows the Newtonian times to coalescence $\tau_n$, Eq. (2.23), computed at the transition frequency (see upper panel) for each class of signals.

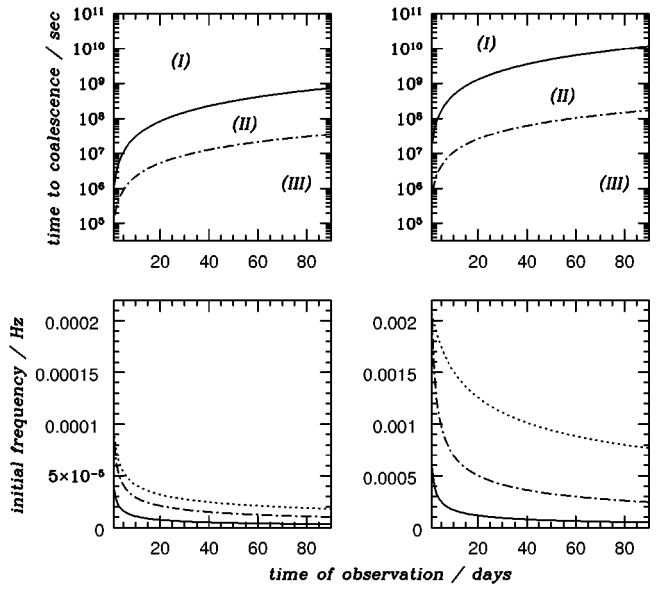


FIG. 2. To show how the partition of signals into different classes depends upon the observation time $T_1$ we consider two binary systems: $M_1=M_2=10^7\,M_\odot$ (left panels) and $M_1=2\times10^6 M_\odot$, $M_2=1000\,M_\odot$ (right panels). The Newtonian time to coalescence $\tau_n$, Eq. (2.23), and the initial frequency $f_b$, Eq. (2.22), are used to separate the classes: solid line between I and II, dash-dotted line between II and III, and dotted line between III and IV. The frequency scale has been chosen so that $f_{\rm isco}$ corresponds to the top of the panel.

As we mentioned in the Introduction, classes I–IV correspond to gravitational wave emission increasingly closer to the final merger and, therefore, to stronger signals. In Fig. 2 we show the frequency $f_b$ and the characteristic time $\tau_n$ that separate the four classes as function of the observation time. For typical present and future data sets (see Table I) and reasonable sources, most signals would show up in class III or IV.

We introduce now the Fourier transform

$$\tilde{h}(f)=\int_{-\infty}^{\infty} e^{-2\pi i f t}h(t)\,dt \tag{2.24}$$

of the real function $h(t)$ and hereafter will work in the more convenient Fourier space. When the frequency $f(t)$ and the amplitude $A(t)$ [Eqs. (2.2) and (2.5)] vary over a time scale much longer than $1/f(t)$ it is convenient to use the *stationary phase approximation* in order to compute the integral (2.24). In our case,

$$\frac{1}{f(t)}\frac{d}{dt}\ln[A(t)]\propto\frac{1}{f(t)}\frac{d}{dt}\ln[f(t)]\propto[\mathcal{M}f(t)]^{5/3}, \tag{2.25}$$

where we have neglected numerical coefficients of proportionality. The evaluation of the actual error involved in this approximation is a delicate matter; however, in the limit

$$[\mathcal{M}f(t)]^{5/3}\ll 1, \tag{2.26}$$

we expect this approximation to be satisfactory for the assessment of the signal-to-noise ratio. Note also that

$$[\mathcal{M}f(t)]^{5/3}<(\mathcal{M}f_{\rm isco})^{5/3}\propto\left(\frac{\mathcal{M}}{M}\right)^{5/3}\propto\eta, \tag{2.27}$$

so that the limit (2.26) is formally satisfied for a small mass ratio. Of course, as usual, the approximation will be fearlessly pushed to the limits of validity.

In the stationary phase approximation to the integral (2.24), for a frequency $f$ only a small interval $\delta t$ contributes around the time $t(f)$ where

$$f(t)=f. \tag{2.28}$$

Note the slight inconsistency of notation: $f$ is now the independent variable in Fourier space, while earlier we have introduced $f(t)$ as a function of time. The time interval is of order

$$\delta t=[\dot{f}(t)]^{-1/2}=\left(\frac{5}{96}\right)^{1/2}\pi^{-4/3}\,\mathcal{M}^{-5/6}\,f^{-11/6}(t), \tag{2.29}$$

corresponding to a local bandwidth $\delta f=1/\delta t$. A finite record in $(0,T_1)$ will pick up only the part of the spectrum between $f_b$ and $f_e$; since dropping the data outside $(0,T_1)$ is equivalent to convolving with $\sin(fT_1)/f$, one wonders how this can

destroy the Fourier components outside $(f_b, f_e)$. The answer is that outside the frequency range defined by $f=f(t)$, $(0 \leqslant t \leqslant T_1)$, the phase of the Fourier integral (2.24) has fast oscillations. The Fourier amplitude is then of order

$$A\,\delta t \approx \frac{\mathcal{M}^{5/6}}{D} f^{-7/6}. \tag{2.30}$$

The full expression of the Fourier transform of $h(t)$, Eq. (2.4), computed according to the stationary phase approximation is [102]

$$\tilde{h}(f) = \begin{cases} \mathcal{A} f^{-7/6} e^{i\Psi(f)}, & f \leqslant f_{\rm isco}, \\ 0, & f > f_{\rm isco}, \end{cases} \tag{2.31}$$

where

$$\mathcal{A} = \left(\frac{5}{6}\right)^{1/2} \frac{1}{4\pi^{2/3}} Q(\iota,\phi) \frac{\mathcal{M}^{5/6}}{D} \tag{2.32}$$

is the amplitude and

$$\Psi(f) = 2\pi f t_n - \Phi_n - \frac{\pi}{4} + \frac{3}{4}(8\pi\mathcal{M}f)^{-5/3} \tag{2.33}$$

the phase.

The existence of an analytic expression of the inspiral signal in Fourier space justifies its use. Compared with the analysis in the time domain, it offers two main advantages: the instrumental response function [see Eqs. (3.1)–(3.4)] is a simple multiplicative factor and we can easily deal with colored noise (see Secs. III and IV).

### B. Final burst

The theoretical knowledge of the signal emitted during the merger of two black holes is at present quite poor. It involves the computation of the solutions of the Einstein equations in highly nonlinear regimes; this issue has currently been tackled by several groups mainly by means of intensive numerical computation on state-of-the-art machines (see [94–96] and references therein). Here we present a simple model for the energy spectral density emitted during the merger, following the approach presented in [103]; although quite naive and crude, it is reasonable for an order of magnitude comparison of the sensitivity of Doppler experiments to inspiral and merger signals, which shall be carried out in Sec. IV.

The wave emitted during the final stages of the life of a binary system is spread over a wide band. For the sake of simplicity, and lack of more detailed knowledge, we assume it to be confined between the final frequency of the inspiral, i.e., $f_{\rm isco}$, and the characteristic frequency $f_{\rm qnm}$ at which the ring-down emission sets in. We will assume

$$f_{\rm qnm} \simeq \frac{1}{2\,\pi\,M} = 3.2\times 10^{-2} \left(\frac{M}{10^6\,M_\odot}\right)^{-1} \text{Hz}, \tag{2.34}$$

which roughly corresponds to the frequency of the quasinormal oscillation for the $l=m=2$ mode of a Kerr black hole with dimensionless spin parameter $|\mathbf{S}|/M^2 \simeq 0.98$, where $\mathbf{S}$ is the spin of the body. This choice of $f_{\rm qnm}$ can be justified as follows: the $l=m=2$ mode, very likely to be excited at the end of the black hole plunge-in, is the one with the longest damping time and the resulting massive black hole will quite probably carry a large intrinsic angular momentum.

Estimating the total energy $E_{\rm merg}$ radiated during the merger phase, in particular its dependence on the (small) mass ratio $\mu/M$, is a delicate matter. We have a transition between the end of the (Newtonian) chirp, with an adiabatic energy loss and a luminosity

$$L = \frac{32}{5} \frac{\mu^2 M^3}{r^5}, \tag{2.35}$$

and an aperiodic trajectory with time scale $\approx M$ and a wideband emission. Neglecting for a moment numerical coefficients, when $r \approx M$ the chirp luminosity is $L=(\mu/M)^2$, corresponding to a radiative amplitude $h_r = \sqrt{L}M/D = \mu/D$. Then one usually assumes that in the transition the luminosity (and the amplitude) do not change their order of magnitude, leading to a radiated energy $E_{\rm merg} = LM = \mu^2/M$ [90,104].

Looking in more detail at the physics, however, the chirp luminosity $L=-dV/2dt$ satisfies the virial theorem in terms of the potential energy $V$. Of course, we do not expect the virial theorem to hold in the plunge phase, but one could say at least that, in order of magnitude, the energy loss is of the order of the decrease in the particle energy, which must be of the order of $\mu M/r = \mu$; this leads to $E_{\rm merg} = \mu$, a large factor $M/\mu$ larger than the previous estimate. The luminosity would be $\mu/M$ and the radiative amplitude would be $\sqrt{\mu M}/D$. This estimate has two problems: there is a large (indeed, unbounded as the mass ratio goes to zero) change in the amplitude; the metric tensor is not analytical in the masses and would not be recoverable in an ordinary perturbation approach. We therefore adopt the first estimate, supported also by extensive numerical and analytical work [103,104]. Note that it implies that during the plunge only a small fraction (of order $\mu/M$ of the total decrease in energy) is radiated away; the rest disappears below the horizon. The radiative power of the two phases is comparable, but the chirp emits more because, when $\mu < M$, it lasts more, by a factor of $M/\mu$. Following [103] and references therein we adopt

$$E_{\rm merg} = k_{\rm merg} \frac{\mu^2}{M}; \tag{2.36}$$

of course, a precise estimate of $k_{\rm merg}$ would require a full numerical calculation, but a reasonable guess yields $k_{\rm merg} \sim 0.16$ [103]. Lacking any evidence about the structure of the energy spectrum, we will make the simple assumption that $E_{\rm merg}$ is uniformly distributed over the band $(f_{\rm qnm}, f_{\rm isco})$, so that

$$\tilde{E}_{\rm merg}(f)=\begin{cases}\dfrac{E_{\rm merg}}{(f_{\rm qnm}-f_{\rm isco})}, & f_{\rm isco}\leqslant f\leqslant f_{\rm qnm},\\ 0, & f<f_{\rm isco}\ \text{ and }\ f>f_{\rm qnm}.\end{cases} \tag{2.37}$$

We recall here that the energy spectrum of the radiation emitted during the inspiral phase is given by

$$\tilde{E}_{\rm insp}(f)=\begin{cases}\dfrac{\pi^{2/3}}{3}\mathcal{M}^{5/3}f^{-1/3}, & f\leqslant f_{\rm isco},\\ 0, & f>f_{\rm isco}.\end{cases} \tag{2.38}$$

Equations (2.37) and (2.38) will enable us to compare the detectability of coalescing binaries during the inspiral and merger phase with Doppler experiments, as the optimal signal-to-noise ratio is simply related to the energy spectrum [see Eq. (4.5)]; this analysis is carried out in Sec. IV.

## III. DOPPLER RESPONSE TO INSPIRAL SIGNALS

In a Doppler experiment, Earth and a spacecraft are used as the end points of a gravitational wave detector [10]. A radio link is transmitted from Earth to the spacecraft, coherently transponded, and sent back to Earth, where, at the time $t$, its frequency is measured with great accuracy; comparing the emitted and received frequency—$\nu_0$ and $\nu(t)$, respectively—one determines the Doppler shift $y(t)=(\nu(t)-\nu_0)/\nu_0$ as a function of time. The contribution to this effect produced by a gravitational wave $h(t)$ is usually called the *Doppler signal* $s(t)$ and reads [10]

$$s(t)=\int_{-\infty}^{\infty}dt'\,r_\theta(t-t')h(t'); \tag{3.1}$$

$$r_\theta(t)=\frac{\cos\theta-1}{2}\,\delta(t)-\cos\theta\,\delta\left(t-\frac{\cos\theta+1}{2}T\right)+\frac{1+\cos\theta}{2}\,\delta(t-T) \tag{3.2}$$

is the characteristic *three-pulse response* of the instrument, as the incoming signal $h(t)$ is repeated in the detector output at three different times (and with different amplitude) $t$, $t-(\cos\theta+1)T/2$, and $t-T$; $r_\theta(t)$ depends on the angle $\theta$ between the spacecraft and the source and the round-trip light time $T=2L$ out to the distance $L$ of the probe. These arise because a gravitational wave pulse meets and affects the photon in the round trip in three events: when the photon leaves the transmitter and returns there after a time $T$ and when it arrives at the spacecraft at the intermediate time $(\cos\theta+1)T/2$. In the frequency domain the Doppler signal (3.1) takes the simple form

$$\tilde{s}(f)=\tilde{r}_\theta(f)\tilde{h}(f), \tag{3.3}$$

where $\tilde{h}(f)$ is given by Eq. (2.31) and the Fourier transform of $r_\theta(t)$ reads

$$\tilde{r}_\theta(f)=\frac{\cos\theta-1}{2}-\cos\theta\exp[\pi i(1+\cos\theta)fT]+\frac{1+\cos\theta}{2}\exp[2\pi ifT]. \tag{3.4}$$

Since the frequency $f$ appears multiplied by the round-trip light time $T$, we introduce the dimensionless variable

$$\xi\equiv fT. \tag{3.5}$$

In agreement with the weak equivalence principle, the response of the instrument goes to zero in the low frequency limit $\xi\ll 1$ (this is the regime in which ground- and space-based interferometers work):

$$\tilde{r}_\theta(\xi)=i\pi\xi\sin^2\theta-\frac{1}{2}\pi^2\xi^2\sin^2\theta(2+\cos\theta)+O(\xi^3). \tag{3.6}$$

To lowest order the angle $\theta$ only affects the coefficient, but not the shape. As $\xi$ increases, $\tilde{r}_\theta(\xi)$ develops modulations in amplitude and, more importantly, in phase, which depend on $\theta$. The beats produced by the superposition of the signals at the times $t$, $t-(\cos\theta+1)T/2$, and $t-T$ result in minima and maxima of the amplitude superimposed to the general increasing trend $A(t)\propto f^{2/3}(t)$ [see Eq. (2.5)] as shown in Fig. 3; they strongly depend on the angle $\theta$ and provide a sensitive signature for its determination.

The transversal character of gravitational waves is reflected in the forward ($|\theta|\ll 1$) and backward ($|\theta'|=|\pi-\theta|\ll 1$) limits, when the wave travels in a direction almost parallel to the Earth-spacecraft line:

$$\tilde{r}_\theta(\xi)=\frac{\theta^2}{4}[(1+2\pi i\xi)e^{2\pi i\xi}-1]+O(\theta^4)\quad(|\theta|\ll 1), \tag{3.7}$$

$$\tilde{r}_\theta(\xi)=\frac{\theta'^2}{4}[e^{2\pi i\xi}-1+2\pi\xi]+O(\theta'^4)\quad(|\theta'|=|\pi-\theta|\ll 1); \tag{3.8}$$

both tend to zero and they have the same limiting amplitude, but different phases. Note that the two limits are not uniform and are violated at high frequency ($\xi\gg 1$).

For generic values of $\theta$ it is convenient to use the squared modulus of Eq. (3.4):

$$|\tilde{r}_\theta(\xi)|^2=\frac{3\cos^2\theta+1}{2}+\frac{\cos^2\theta-1}{2}\cos(2\pi\xi)-\cos\theta(\cos\theta+1)\cos[(\cos\theta-1)\pi\xi]-\cos\theta(\cos\theta-1)\cos[(\cos\theta+1)\pi\xi], \tag{3.9}$$

which, in the limit $\xi\ll 1$, reads

$$|\tilde{r}_\theta(\xi)|^2=\pi^2\xi^2\sin^4\theta\left[1-\frac{1}{3}\left(1-\frac{1}{4}\cos^2\theta\right)\pi^2\xi^2\right]+O(\xi^5). \tag{3.10}$$

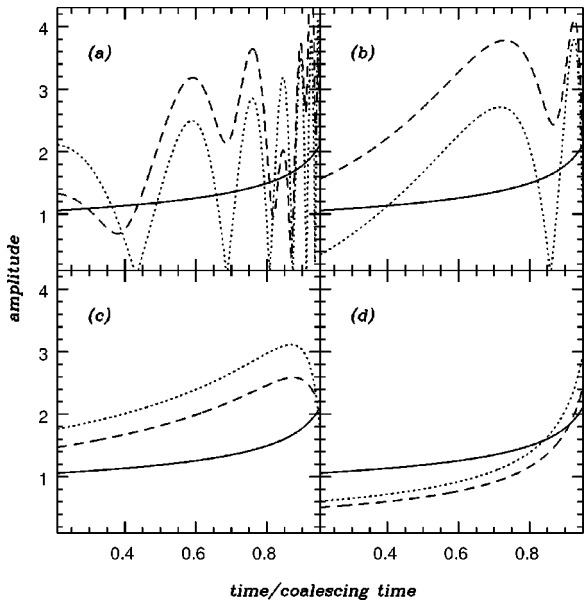


FIG. 3. The effect of the Doppler filter $r_\theta$ on inspiral signals. The plots show a comparison between the chirp amplitude $A(t)$, Eq. (2.5) (solid line), and the Doppler amplitude for different values of the angle $\theta$ ($\cos\theta=0$, dashed line; $\cos\theta=0.4$, dotted line) and of the chirp mass: (a) $\mathcal{M}=10^5\,M_\odot$, (b) $\mathcal{M}=10^6\,M_\odot$, (c) $\mathcal{M}=10^7\,M_\odot$, (d) $\mathcal{M}=10^8\,M_\odot$ ($\eta=1/4$ for all systems). The chirp amplitudes are normalized to $A(t=0)=1$; the round-trip light time is $T=4000$ sec. Note the increasing modulation induced by the Doppler response as the final merger is approached; this modulation disappears as $\mathcal{M}/T$ increases because the filter degenerates in a multiplicative factor [cf. Eq. (3.6) and Fig. 4].

$|\tilde r_\theta(\xi)|^2$, shown in Fig. 4, is an even function of $\cos\theta$ and sum of four functions periodic in $\xi$, with frequencies 0, 1, $(1-\cos\theta)/2$, and $(1+\cos\theta)/2$, respectively. Its average is $(3\cos^2\theta+1)/2$. As an example, for $\theta\to\pi/2$ the response reads

$$|\tilde r_\theta(\xi)|^2=\sin^2(\pi\xi)+[(1-\cos(\pi\xi))^2-2\pi\xi\sin(\pi\xi)]\times\left(\theta-\frac{\pi}{2}\right)^2+O\left[\left(\theta-\frac{\pi}{2}\right)^4\right] \tag{3.11}$$

and it has a maximum for $\xi=1/3$. For large frequencies it develops more and more lobes with angular scale $1/\xi$ (see Fig. 4). Averaging $|\tilde r_\theta(\xi)|^2$ over the direction $\theta$ one obtains the mean square response of the detector:

$$\overline{|\tilde r_\theta(\xi)|^2}=\frac{1}{2}\int_{-1}^{1}|\tilde r_\theta(\xi)|^2\,d(\cos\theta)=\frac{\pi^2\xi^2-3}{\pi^2\xi^2}-\frac{\pi^2\xi^2+3}{3\pi^2\xi^2}\cos(2\pi\xi)+\frac{2}{\pi^3\xi^3}\sin(2\pi\xi), \tag{3.12}$$

which, in the low and high frequency limit, reads

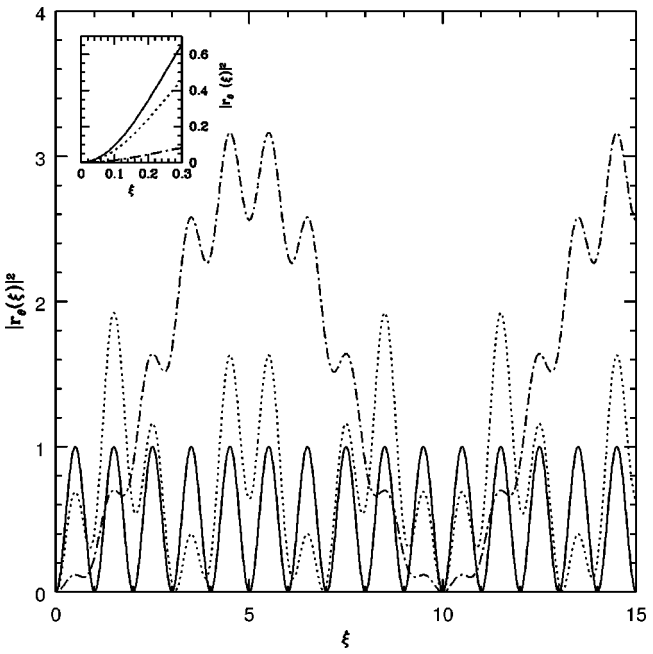


FIG. 4. The square modulus of the Doppler filter $|\tilde r_\theta(\xi)|^2$, Eq. (3.9), as a function of $\xi\equiv f\,T$ for selected values of the angle $\theta$ (solid line, $\cos\theta=0$; dotted line, $\cos\theta=0.4$; dot-dashed line, $\cos\theta=0.8$). The small box zooms the behavior of $|\tilde r_\theta(\xi)|^2$ for $\xi\ll1$; note that, only when $\xi$ is small, $|\tilde r_\theta(\xi)|^2$ is a monotonic decreasing function of $\cos\theta$, which is not true for $\xi\gtrsim1$.

$$\overline{|\tilde r_\theta(\xi)|^2}=\begin{cases}\dfrac{8}{15}\pi^2\xi^2\left(1-\dfrac{29}{84}\pi^2\xi^2\right)+O(\xi^6) & (\xi\ll1),\\[2ex] 1-\dfrac{1}{3}\cos(2\pi\xi) & (\xi\gg1).\end{cases} \tag{3.13}$$

During an experiment neither the angle $\theta$ nor the round-trip light time $T$ is exactly constant, mainly due to the motion of Earth; their time variation induces changes in the phase of the filter of order $\pi\Delta\theta fT$ and $\pi f\Delta T$. For the latter $\Delta T\approx 2\,v_\oplus T_1/c\approx 2\times10^{-4}T_1$ ($v_\oplus\simeq30$ km/sec is the orbital velocity of Earth) and the effect is relevant when

$$2\times10^{-4}\pi fT_1\approx1; \tag{3.14}$$

the angle $\theta$ affects the phase by a smaller amount. For CASSINI experiments this occurs at about 5 mHz, which is above the most important sensitivity region of the instrument (see next section). We will therefore consider constant both $T$ and $\theta$.

## IV. SENSITIVITY OF DOPPLER EXPERIMENTS

The Fourier output of the detector,

$$\tilde y(f)=\tilde s(f)+\tilde n(f), \tag{4.1}$$

is the sum of the signal $\tilde s(f)$ and the noise $\tilde n(f)$. The noise is assumed to be stationary, with zero mean and spectral power density

$$\langle \tilde{n}^*(f)\tilde{n}(f')\rangle = \delta(f-f')S_n(f). \tag{4.2}$$

We consider single-sided noise spectra $S_n(f)$, formally from 0 to $+\infty$, and take into account the finite instrumental bandwidth with suitably large values at the boundaries of the sensitivity window. When $S_n(f)$ is white the corresponding *Allan deviation* [105]

$$\sigma_y = \sqrt{\frac{S_n}{\tau}} \tag{4.3}$$

is inversely proportional to the square root of the integration time $\tau$; for colored spectra, see, e.g., [106]. For simplicity we use a continuous spectrum $S_n(f)$, although, over an experiment of duration $T_1$ and with sampling time $\Delta_s$, the spectrum consists of discrete Fourier modes spaced by $1/T_1$, from $1/T_1$ to the Nyquist frequency $1/(2\Delta_s)$.

Since the shape of the signal in the inspiral phase can be accurately predicted, the technique of *matched filtering* is particularly suitable (see, e.g., [73,74] and references therein). It can be shown that if the signal $\tilde{s}(f)$ is known to within a constant (and real) amplitude $h$, its least squares estimator has a variance given by

$$\left(\frac{s}{\sigma_n}\right)^2 = \rho^2 = 4\int_0^\infty \frac{|\tilde{s}(f)|^2}{S_n(f)}\,df. \tag{4.4}$$

The quantity $\rho$ is appropriately called the *signal-to-noise ratio* and is related to the energy spectrum of the radiation $\tilde{E}(f)$ by the relation

$$\rho^2 \propto \frac{1}{D^2}\int_0^\infty \frac{|\tilde{r}_\theta(f)|^2}{f^2 S_n(f)}\,\tilde{E}(f)\,df. \tag{4.5}$$

It is useful to introduce an ideal reference value of the SNR and to discuss its dependence on the main parameters. From Eq. (3.13), we can approximate the instrumental filter $r_\theta$, as follows:

$$|\tilde{r}_\theta(\xi)|^2 \sim \begin{cases} \xi^2 & (\xi<1), \\ 1 & (\xi>1). \end{cases} \tag{4.6}$$

With a white noise spectrum $S_n = \sigma_y^2\tau = \text{const}$, and taking into account the frequency dependence of the signal [see Eqs. (2.31), (3.3), and (4.6)], we have

$$\frac{|\tilde{s}(f)|^2}{S_n(f)} \propto \begin{cases} \dfrac{\xi^{-1/3}}{\sigma_y^2\tau} & (\xi<1), \\ \dfrac{\xi^{-7/3}}{\sigma_y^2\tau} & (\xi>1). \end{cases} \tag{4.7}$$

This is a decreasing function of $\xi$; both sides are integrable, so that in this ideal case the bulk of the sensitivity comes from $f\sim 1/T$ (cf. also Fig. 7). We can define the *ideal* SNR by taking $\xi_b \equiv f_b T \ll 1$, $\xi_e \equiv f_e T \gg 1$, and the direction angle $\theta=\pi/2$, for which $|\tilde{r}_{\pi/2}(\xi)|^2 = \sin^2(\pi\xi)$; from Eqs. (2.31), (2.32), and (4.4), averaging over the source angles $\iota,\varphi$, we get

$$\rho_{\rm id}^2 = K\frac{T^{4/3}\mathcal{M}^{5/3}}{\sigma_y^2\tau D^2}, \tag{4.8}$$

where

$$K \equiv \frac{5}{24\pi^{4/3}}\frac{\langle Q^2(\iota,\varphi)\rangle}{T^{4/3}}\int_0^\infty f^{-7/3}|\tilde{r}_{\pi/2}(f)|^2\,df$$

$$= \frac{2^{1/3}\pi}{3^{3/2}\Gamma(7/3)} \simeq 0.64. \tag{4.9}$$

The ideal *ken*—the largest distance at which a source is ideally detectable at $\rho_{\rm id}=1$—is

$$D_{\rm id} = K^{1/2}\frac{T^{2/3}\mathcal{M}^{5/6}}{\sigma_y\sqrt{\tau}}. \tag{4.10}$$

For the CASSINI mission (see Table I), with $T=10^4$ sec and $\sigma_y^2\tau = 9\times 10^{-26}$ Hz$^{-1}$, it has the value

$$D_{\rm id} \simeq 45\left(\frac{\mathcal{M}}{10^6 M_\odot}\right)^{5/6}\left(\frac{T}{10^4\ \text{sec}}\right)^{2/3} \times\left(\frac{\sigma_y^2\tau}{9\times 10^{-26}\ \text{Hz}^{-1}}\right)^{-1/2}\ \text{Mpc}. \tag{4.11}$$

For ULYSSES the ideal ken for $\mathcal{M}=10^6 M_\odot$ is $\simeq 3$ Mpc; in the coincidence experiment, the values for GALILEO and Mars Observer are $\simeq 0.5$ Mpc and $\simeq 2$ Mpc, respectively, where the values of $\sigma_y, \tau$, and $T$ have been chosen according to Table I.

The ideal value (4.8) for the SNR neglects several degradation factors of real experiments, including (1) the direction of the source may be unfavorable, (2) the frequency interval $(f_b, f_e)$ swept by the signal is finite because the record has a finite length and the instrument has its own cutoffs, and (3) the noise spectrum is generally red, which damages the SNR in the critical low frequency band.

Only experiments can provide a safe estimate of the noise structure, especially when aiming at high sensitivities or wide frequency windows. The sensitivity of past Doppler experiments was limited mostly by phase noise due to interplanetary plasma turbulence, whose spectrum is well modeled by a power law $S_n(f)\propto f^{-p}$ with $p$ close to the Kolmogorov value (2/3). The higher frequencies (typically above $10^{-1}$ Hz) are dominated by the white phase thermal noise of the receivers, with a spectrum proportional to $f^2$. At the opposite end of the observation window ($f<1/T$), several effects come into play and the spectral characteristics of the noise are more uncertain. In general the functional dependence of the noise spectrum becomes very sensitive to the data processing, in particular to calibrations for the ionosphere and, to a lesser extent, the static troposphere. Inaccu-

rate modeling of the relative motion between the tracking station and the spacecraft is an additional source of noise at low frequencies. As the response of a Doppler detector to gravitational signals decreases (spectralwise) as $1/f^2$, there was little interest in extending the observation window at low frequencies and in general the time series of past experiments were high-pass filtered with cutoff frequencies slightly lower than $1/T$. However, in order to understand better the behavior of the Doppler noise at frequencies below $1/T$, the Doppler residuals from the ULYSSES 1992 experiment were also analyzed by making use of the available trajectory and media calibration data, without any free parameter to be fitted for. The resulting power spectrum was a power law with spectral index approximately equal to $-2$. A better orbital determination and a more accurate modeling of media effects is likely to decrease significantly the noise at low frequencies and make its functional dependence on frequencies weaker.

The structure of the noise changes significantly for the CASSINI experiments. Interplanetary and ionospheric plasma give negligible contributions, while the main limitation is due to tropospheric water vapor ($S_n \propto f^{-p}$, $0.4<p<0.6$). Keeping this noise source at levels below $1.5\times10^{-15}$ at time scales between $10^3$ and $10^4$ sec requires knowledge of the water-vapor-integrated content accurate to 10%. Such an unprecedented accuracy will be made possible thanks to a new, advanced water vapor radiometer expressly developed for CASSINI experiments. Significant contributions to the noise are expected from the frequency standard and the antenna mechanical motions, especially wind loading. Thanks to the very high SNR, the thermal noise becomes relevant only at very high frequencies (about 1 Hz).

The noise spectral density can be therefore approximated with a simple analytical expression made up with three power law contributions:

$$S_n(f)=S_0\sum_{j=1}^{3}\left(\frac{f}{f_j}\right)^{\alpha_j}, \tag{4.12}$$

where

$$S_0=S_n(1/T)=\sigma_y^2(T)T \tag{4.13}$$

sets the spectral level; the frequencies $f_j$ and the exponents $\alpha_j$, satisfying

$$\sum_{j=1}^{3}(T f_j)^{-\alpha_j}=1, \tag{4.14}$$

characterize the different contributions to the noise. We can define the transition frequencies $f_{12}$ and $f_{23}$ as the intercept between two power approximations; for example, the transition frequency $f_{12}$ between regions 1 and 2 (characterized by the indices $\alpha_1$ and $\alpha_2$, respectively) is given by

$$\left(\frac{f_{12}}{f_1}\right)^{\alpha_1}=\left(\frac{f_{12}}{f_2}\right)^{\alpha_2}. \tag{4.15}$$

In the case of ULYSSES, high frequencies (dominated by thermal noise) are strongly perturbed by the spacecraft rotational dynamics, so that the data have been actually low-pass filtered to $5\times10^{-2}$ Hz$=f_{23}$, and we can assume $\alpha_3\gg1$, formally achieved by setting $\alpha_3=10$. The frequency window between $f_{12}\simeq1/T$ and $f_{23}$ can be characterized by a power law with index $\alpha_2\approx-0.5$, due to propagation noise [14,15]. Below $\approx1/T=f_{12}$ the procedure for the generation of residuals essentially cuts off all frequencies and we have formally assumed a low frequency spectral index $\alpha_1=-10$ (see Table II).

TABLE II. Characteristic parameters of the ULYSSES and CASSINI noise spectral density. The table shows the reference frequency $1/T$; the reference noise spectral density level $S_0=S_n(1/T)$; the transition frequencies $f_{12}, f_{23}$; the exponents $\alpha_j$; and the frequencies $f_j$ $(j=1,2,3)$ of each regime; see Eqs. (4.12)–(4.14). When, as in our case, $T f_{12}=1$, $T f_{23}\gg1$ and $\alpha_3>\alpha_2$, then $Tf_1=2^{1/\alpha_1}$, $Tf_2=2^{1/\alpha_2}$, and $Tf_3=Tf_{23}2^{1/\alpha_3}(Tf_{23})^{-\alpha_2/\alpha_3}$.

| Parameters | ULYSSES | CASSINI |
|---|---|---|
| $(1/T)$/Hz | $2\times10^{-4}$ | $10^{-4}$ |
| $S_0$/Hz$^{-1}$ | $2.5\times10^{-24}$ | $9\times10^{-26}$ |
| $f_{12}$/Hz | $2\times10^{-4}$ | $10^{-4}$ |
| $f_{23}$/Hz | $5\times10^{-2}$ | $10^{-1}$ |
| $f_1$/Hz | $2\times10^{-4}$ | $7.07\times10^{-5}$ |
| $f_2$/Hz | $8\times10^{-4}$ | $2.5\times10^{-5}$ |
| $f_3$/Hz | $5\times10^{-2}$ | $7.95\times10^{-1}$ |
| $\alpha_1$ | $-10$ | $-2$ |
| $\alpha_2$ | $-1/2$ | $-1/2$ |
| $\alpha_3$ | 10 | 2 |

As we have already anticipated in the Introduction (and we shall show more in detail in the next sections), one of the main conclusions of this paper is that low frequencies (i.e., $\lesssim1/T$) are crucial to achieving a large SNR and to widening the range of accessible masses. As we said, the noise spectrum for $fT\lesssim1$ is to a large extent unknown, as systematic effects, mostly related to the orbit determination process and the tropospheric correction, are likely to come into play. For the goal of assessing the expected SNR for CASSINI we take the view that these systematic effects do not exceed the propagation noise above $10^{-4}$ Hz and keep $\alpha_2=-0.5$. The level $S_0$ is given by the main specification for the Allan deviation, i.e., $\sigma_y=3\times10^{-15}$ at $10^4$ sec, corresponding to $S_n(10^{-4}\ \text{Hz})=9\times10^{-26}$ sec; we also limit our band to a minimum frequency of $10^{-6}$ Hz. For the interval up to $f_{12}=10^{-4}$ Hz the only experimental evidence comes from ULYSSES data and, accordingly, we chose $\alpha_1=-2$; this value, however, is conservative, as in the processing of ULYSSES data no particular attention was paid to the reduction of the noise below $10^{-4}$ Hz. The effect of possible different values of $\alpha_1$ will be explored in Sec. IV A. Thermal noise, with $\alpha_3=2$, can be expected to set in at a frequencies higher than $\sim0.1$ Hz; however, the limited sampling time will prevent to go much beyond. In Fig. 5 we show the noise

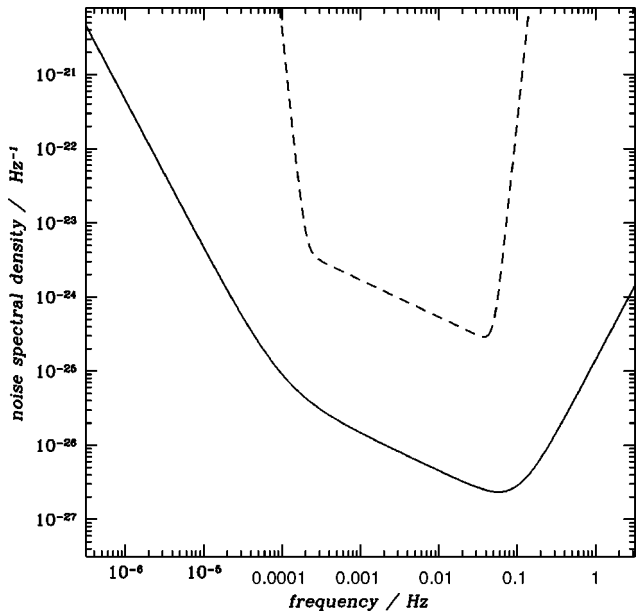


FIG. 5. Noise spectral density of CASSINI (solid line) and ULYSSES (dashed line). $S_n(f)$ is computed according to Eqs. (4.12)–(4.15) and Table II.

spectral density of CASSINI and ULYSSES, computed using Eqs. (4.12) and (4.13) with the parameters given in Table II.

Keeping $S_0$ and the frequencies $f_j$ $(j=1,2,3)$ fixed, we now write the SNR in the form

$$\rho^2 = K \frac{\mathcal{M}^{5/3} T^{4/3}}{S_0 D^2} \Upsilon(\xi_b, \xi_e, \theta; \alpha_j). \tag{4.16}$$

The *sensitivity function* $\Upsilon$

$$\Upsilon(\xi_b, \xi_e, \theta; \alpha_j) \equiv K^{-1} \left\{ \int_{\xi_b}^{\xi_e} \xi^{-7/3} \left[ \sum_j \left( \frac{\xi}{\xi_j} \right)^{\alpha_j} \right]^{-1} |\tilde{r}_\theta(\xi)|^2 \, d\xi \right\} \tag{4.17}$$

measures the change of SNR with respect to the ''ideal'' case, Eq. (4.8), and satisfies

$$\Upsilon(0, \infty, \pi/2; 0) = 1. \tag{4.18}$$

Generally this function is less than unity and gives a degradation; we must, however, point out that the value $\pi/2$ for the angle $\theta$ is not always (i.e., for any arbitrary choice of $\alpha_j$) the best; furthermore, we have defined the ''white noise'' considering the level of the real noise at $f=1/T$, so that $S_n(f)$ may actually be smaller than the white noise for $f > 1/T$. Notice also that when $\alpha_1 \geqslant -2/3$ the SNR spectral density is not integrable and the total SNR is dominated by the low frequency end $f_b$.

The crucial physical parameter of a binary is its chirp mass $\mathcal{M}$, which characterizes the rate of change of the gravitational wave frequency and, from Eqs. (2.15) and (2.16), sets the relationship (except for class IV)

$$\mathcal{M} = \frac{5^{3/5}}{(8\pi)^{8/5}} T_1^{-3/5} f_b^{-8/5} \left[ 1 - \left( \frac{f_b}{f_e} \right)^{8/3} \right]^{3/5} = \mathcal{M}_c \left[ 1 - \left( \frac{f_b}{f_e} \right)^{8/3} \right]^{3/5} \quad \text{(class I–III)}. \tag{4.19}$$

We see that, given $f_b$ and $T_1$, there is a critical value of the chirp mass

$$\mathcal{M}_c = \frac{5^{3/5}}{(8\pi)^{8/5}} T_1^{-3/5} f_b^{-8/5} \simeq 9.2 \times 10^5 \left( \frac{f_b}{10^{-4}\,\mathrm{Hz}} \right)^{-8/5} \left( \frac{T_1}{40\,\mathrm{days}} \right)^{-3/5} M_\odot, \tag{4.20}$$

above which, in class I–III, no measurement is possible. At this critical value, when $f_b \ll f_{\mathrm{isco}}, T_1$ basically coincides with the time to coalescence, $\tau_c$ [Eq. (2.17)].

When $\mathcal{M} \ll \mathcal{M}_c$, the detected signal is intrinsically narrow band; the fractional bandwidth

$$\Delta = \frac{f_e - f_b}{f_b} \tag{4.21}$$

is small and given by

$$\Delta = \frac{3}{8} \left( \frac{\mathcal{M}}{\mathcal{M}_c} \right)^{5/3} = \frac{3}{8} \frac{T_1}{\tau_c}. \tag{4.22}$$

This case, in which there is little power and information, is less interesting.

When the data set includes the merger (class IV), instead of Eq. (4.19) we have

$$\mathcal{M} = \mathcal{M}_c \left\{ \frac{T_1}{\tau_c} \left[ 1 - \left( \frac{f_b}{f_{\mathrm{isco}}} \right)^{8/3} \right] \right\}^{3/5} \quad \text{(class IV)}. \tag{4.23}$$

The coefficient within square brackets can be greater than unity, so that the inequality $\mathcal{M} < \mathcal{M}_c$ does not apply.

Since, with decreasing frequency, the spectral density of the SNR decreases or has a weaker growth below $1/T$, it is very convenient to have $T f_b < 1$. When $\xi_e = f_e T \ll 1$ the response $i\pi\xi \sin^2\theta$, Eq. (3.6), weakens the signal. When $\xi_e > 1$ the response introduces strong modulations that depend on $\theta$ and we have full sensitivity. This is the interesting region and will be explored in Sec. IV A using the dynamical behavior of the source.

Before discussing in detail the behavior of the SNR in observations of inspiral signals as a function of the relevant parameters, it is instructive to compare the SNR of Doppler experiments on the inspiral and merger phase. If $\rho_{\mathrm{insp}}$ and $\rho_{\mathrm{merg}}$ correspond to the optimal SNR achievable by observations of the same source in the two regimes, from Eq. (4.5) we can write

$$\frac{\rho_{\rm insp}}{\rho_{\rm merg}}=\left[\frac{\displaystyle\int_{f_{\rm B}}^{f_{\rm isco}}\frac{\overline{|\tilde r_\theta(f)|^2}}{f^2\,S_n(f)}\tilde E_{\rm insp}(f)\,df}{\displaystyle\int_{f_{\rm isco}}^{f_{\rm qnm}}\frac{\overline{|\tilde r_\theta(f)|^2}}{f^2\,S_n(f)}\tilde E_{\rm merg}(f)\,df}\right]^{1/2}. \qquad (4.24)$$

We stress that in the previous relationship we have assumed optimal filtering not only for the inspiral but also for the merger signal; if for the former the assumption is realistic (cf. [107]), for the latter it is indeed very optimistic. Notice also that $\rho_{\rm insp}$ is the largest SNR obtainable for a chirp, as we integrate over the widest frequency band $(f_B, f_{\rm isco})$ for a data set of length $T_1$ (cf. Sec. IV A), and we have averaged the three-pulse response function over the angle $\theta$; cf. Eq (3.12). For a given source, if $(\rho_{\rm insp}/\rho_{\rm merg})>1$ $(<1)$, it is therefore ''more convenient'' to search for it by means of observations of the inspiral (merger) signal.

Inserting into Eq. (4.24) the flat spectrum (2.37) for $\tilde E_{\rm merg}(f)$ and (2.38) for $\tilde E_{\rm insp}(f)$, the ratio of SNR's becomes

$$\frac{\rho_{\rm insp}}{\rho_{\rm merg}}\simeq 1.1\,J\left(\frac{k_{\rm merg}}{0.16}\right)^{-1/2}\left(\frac{T}{10^4\,\sec}\right)^{1/6}\times\left(\frac{M}{2\times10^7\,M_\odot}\right)^{1/3}\left(\frac{\mu}{5\times10^6\,M_\odot}\right)^{-1/2}, \qquad (4.25)$$

where

$$J\equiv\left[\frac{\displaystyle\int_{Tf_{\rm B}}^{Tf_{\rm isco}}\frac{\overline{|\tilde r_\theta(\xi)|^2}}{\xi^{7/3}\,S_n(\xi)}d\xi}{\displaystyle\int_{Tf_{\rm isco}}^{Tf_{\rm qnm}}\frac{\overline{|\tilde r_\theta(\xi)|^2}}{\xi^{2}\,S_n(\xi)}d\xi}\right]^{1/2} \qquad (4.26)$$

measures the relative overlap of the inspiral and merger signals with respect to the instrument response. In Fig. 6 we show $(\rho_{\rm insp}/\rho_{\rm merg})$ and $J$ as a function of the chirp mass for two different mass ratios, 1 and 0.01, for a nominal CASSINI experiment of 40 days with $S_n(f)$ given by Eqs. (4.12)–(4.14). The value of the chirp mass $\mathcal{M}\sim10^7\,M_\odot$ (for a low frequency cutoff of $10^{-6}$ Hz) sets the transition: for $\mathcal{M}>10^7\,M_\odot$, $\rho_{\rm merg}$ rapidly exceeds $\rho_{\rm insp}$ by a factor $\sim10$ or more. The drop of the ratio $\rho_{\rm insp}/\rho_{\rm merg}$ is due to the fact that with large chirp masses progressively greater parts of the inspiral signal lay outside the sensitivity range. Assuming a low frequency cutoff of around $10^{-4}$ Hz, as done in past experiments, the transition occurs at a lower value of $\mathcal{M}\simeq5\times10^6\,M_\odot$ and the drop of $(\rho_{\rm insp}/\rho_{\rm merg})$ is much steeper. As a consequence, for $\mathcal{M}\lesssim10^7\,M_\odot$ the neglect of the merger signal in searching templates is not serious; for $\mathcal{M}\gtrsim10^7\,M_\odot$ coherent search techniques that include merger waveforms would rapidly increase the instrument range of sight, by more than one order of magnitude. However, at present, our poor knowledge of the burst waveform makes it of little use in the search. Only coincidence experiments can offer a chance of carrying out such searches; this work is currently in progress—under the assumption of very simple shapes of the waves—for the analysis of data recorded in coincidence during the tracking of ULYSSES, Mars Observer, and GALILEO [16].

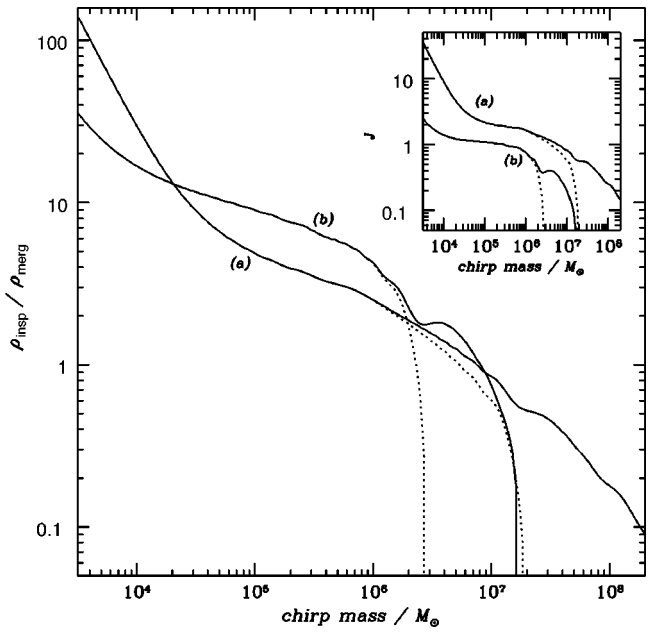


FIG. 6. Comparison of the sensitivity of CASSINI experiments in observations of inspiral and merger signals. For a given source, the plot shows the ratio of the two optimal SNR's as a function of the chirp mass and for the mass ratios 1 and 0.01, labelled (a) and (b), respectively. The solid and the dotted lines refer, respectively, to the low frequency cutoff of $10^{-6}$ Hz and $10^{-4}$ Hz. The small box shows, for the same cases, the relative overlap $J$, Eq. (4.26), of the inspiral and merger signal with respect to the instrument response. The time of observation is assumed to be $T_1=40$ days and the noise spectral density $S_n(f)$ is computed according to Eqs. (4.12)–(4.15) and Table II.

### A. Sensitivity function

In this section we discuss the dependence of the sensitivity function $\Upsilon(\xi_b,\xi_e,\theta;\alpha_j)$ on the main parameters that characterize the inspiral signal and the instrument, in particular the possible causes of degradation from the ideal value.

To illustrate the first reason of degradation—the unfavorable angle $\theta$—as well as the behavior of $\Upsilon$ depending on the frequency range swept by the signal during the observation time, we show in Fig. 7 the spectral sensitivity function $\tilde\Upsilon(f)$ for CASSINI's nominal noise (see Fig. 5 and Table II). Its peak lies in the interval $0.1\lesssim\xi\lesssim1$, broadening and diminishing as $\cos\theta$ increases. For $\xi\ll1$, $\tilde\Upsilon(f)$ is a monotonic, decreasing function of $\cos\theta$, while as $\xi$ exceeds unity, oscillations of increasing frequency occur. The overall effect of the angle $\theta$ is given by the function $\Upsilon(\xi_e=0,\ \xi_b=\infty,\theta;\alpha_1)$, plotted in Fig. 8, where we also keep $\alpha_1$ as a free parameter in order to show the effect of the redness of the noise spectral density at low frequencies (that is, $f\lesssim1/T$); for $\alpha_1\gtrsim-0.9$, $\Upsilon(\xi_e=0,\ \xi_b=\infty,\theta;\alpha_1)$ has a maximum at the ex-

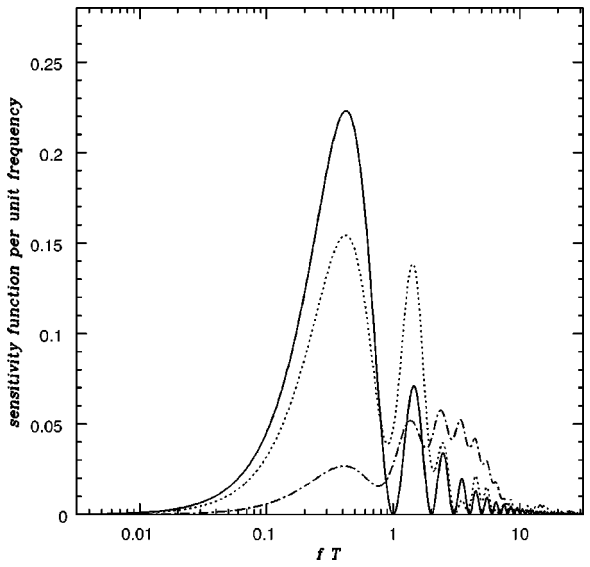


FIG. 7. The spectrum $\tilde{\Upsilon}(f)$ of the sensitivity function; see Eq. (4.17). We have used the CASSINI noise parameters, Table II and Fig. 5 (solid line, $\cos\theta=0$; dotted line, $\cos\theta=0.4$; dot-dashed line, $\cos\theta=0.8$).

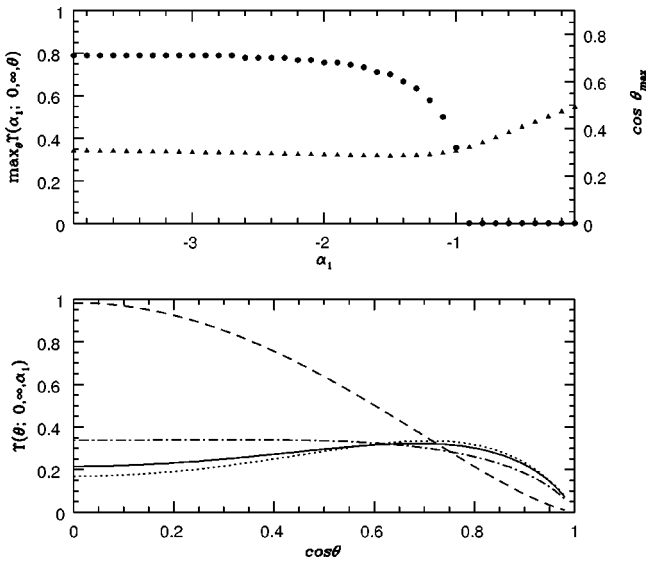


FIG. 8. The deterioration of the sensitivity function $\Upsilon$, and therefore of the SNR, due to the angle $\theta$ between the source and the probe and the redness of the spectrum at low frequencies, given by $\alpha_1$ [cf. Eqs. (4.12)–(4.15) and Table II], as described by the function $\Upsilon(\xi_e=0,\ \xi_b=\infty,\theta;\alpha_1)$. In the upper panel we show, as a function of $\alpha_1$, the maximum value of $\Upsilon(\xi_e=0,\ \xi_b=\infty,\theta;\alpha_1)$ (triangles) and the angle $\theta_{\max}$ (circles) at which it is attained. The ''normal'' value $\theta_{\max}=\pi/2$ occurs above $\alpha_1\simeq-0.9$. The lower panel shows the behavior of $\Upsilon(\xi_e=0,\ \xi_b=\infty,\theta;\alpha_1)$ as a function of $\cos\theta$ for the case $\alpha_1=0$ (dashed line), $\alpha_1=-1$ (dot-dashed line), $\alpha_1=-2$ (solid line), and $\alpha_1=-3$ (dotted line); the values of $\alpha_2$ and $\alpha_3$ are $-1/2$ and $+2$, respectively, corresponding to those of the CASSINI experiments. Note that, for $\alpha_1\lesssim-1$, the smallest deterioration does not occur at the obvious value $\cos\theta=0$; in particular, for $\alpha_1=-2$ it occurs at $\cos\theta\simeq0.68$, so that a small signal enhancement with respect to the ideal case is possible.

pected value $\cos\theta=0$. This is not true anymore for redder spectra, and the value of $\cos\theta$ at which $\Upsilon$ reaches the maximum depends on $\alpha_1$; for $\alpha_1=-2$ it corresponds to $\cos\theta\simeq0.68$.

Concerning the second reason for degradation—the limited bandwidth of the signal—we show first (Fig. 9) the effect of $f_b$ and $f_e$. The deterioration can be strong: $\Upsilon$ can significantly deviate (by one order of magnitude or more) from the ideal value. When both $\xi_b$ and $\xi_e$ are $\lesssim1$, $\Upsilon$ is a smooth function of $f_b$ and $f_e$, but as soon as they enter the region $f\gtrsim1/T$, there are oscillations. We have used here (and later) the ''nominal'' CASSINI form of the noise spectrum (Fig. 5).

It is interesting to investigate $\Upsilon$ in relation to relevant astrophysical parameters. We concentrate on four fiducial ''best'' sources defined by choosing the initial frequency $f_b$ and assuming that the coalescence occurs at the end of the record, so that $f_b=f_B$ and $f_e=f_{\rm isco}$. Each of them is a binary with equal masses ($\eta=1/4$), which determines the chirp mass in terms of the critical chirp mass for a nominal run of 40 days; see Eq. (4.20). This sets also the final frequency $f_e=f_{\rm isco}$ and the number of wave cycles recorded at the detector. Table III summarizes the main properties of the fiducial sources. In all four cases $f_e\gg f_b$, so that we have a wideband search and the source's chirp mass is only slightly smaller than the critical value.

Keeping $f_b$ and $\mathcal{M}$ fixed, we first study the effect of $T_1$ on $\Upsilon$. As $T_1$ decreases, the signal becomes of class III and we lose a progressively greater part of its end. Using the same chirp mass, the final frequency $f_e$ decreases according to Eq. (2.15). This progressive restriction of the search bandwidth is responsible for the great deterioration in SNR (Fig. 10). Since we have assumed that there is no signal beyond the coalescence frequency $f_{\rm isco}$, the sensitivity function remains constant for $T_1>40$ days.

In Fig. 11 we show how the sensitivity function is affected by the round-trip light time $T$ for the same fiducial sources (and with a run of 40 days). The variation of $T$ shifts the response function—Eq. (3.9) and Fig. 4—in relation to the search band $(f_b,f_e)$. The deterioration with increasing $T$ is due to the fact that $\xi_e$ becomes smaller than unity and one loses signal in the high frequency side.

Finally, in Fig. 12 we investigate the effect of $f_b$ on $\Upsilon$; for each value of $f_b$, we have computed the corresponding critical chirp mass (4.20) for a 40-day experiment and then evaluated the sensitivity function for three different sources' orientations in the sky; essentially, for each $f_b$ we tune the observation on the mass that produces the highest SNR. The largest values of $\Upsilon$ are achieved for $10^{-5}\,{\rm Hz}\lesssim f_b\lesssim10^{-3}\,{\rm Hz}$, corresponding to $10^4\,M_\odot\lesssim\mathcal{M}_c\lesssim10^8\,M_\odot$.

### B. Sensitivity of past and future Doppler experiment

In this section we analyze the sensitivity of Doppler experiments—in particular CASSINI—for inspiral signals; we estimate the achievable signal-to-noise ratio as function of the chirp mass $\mathcal{M}$ and the initial frequency $f_b$ (as well as the mass ratio). We consider in detail two targets, the Virgo cluster ($D\simeq17$ Mpc) and the galactic center ($D\simeq8$ kpc);

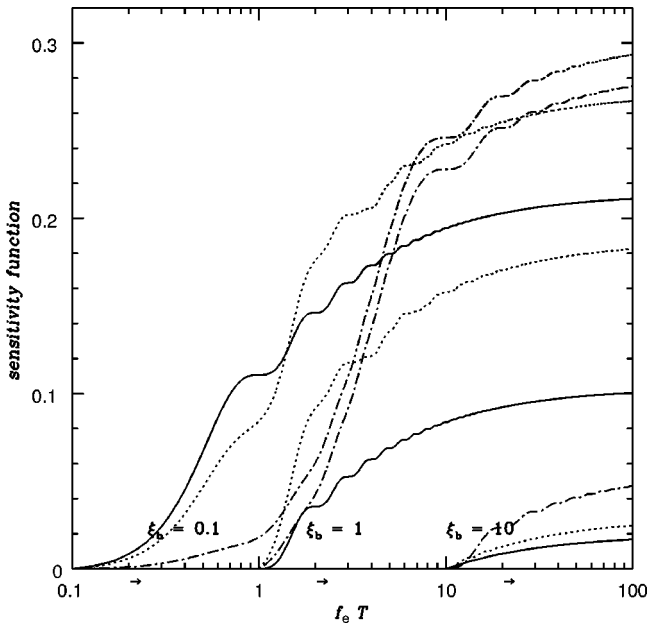


FIG. 9. The behavior of the sensitivity function $\Upsilon$ as a function of the final frequency $f_e$ (in units of the round-trip light time $T$) for selected values of the initial frequency $T\,f_b=\xi_b=0.1,1,10$ (see labels). The CASSINI noise parameters have been used (Table II and Fig. 5). To the right of the arrows we have broad band searches with $f_e-f_b>f_b$ (solid line, $\cos\theta=0$; dotted line, $\cos\theta=0.4$; dot-dashed line, $\cos\theta=0.8$).

the results are presented so that they can be scaled to an arbitrary distance and location in the sky.

CASSINI will perform three experiments, each lasting 40 days at the epoch of three solar oppositions, i.e., when the Sun, Earth, and the probe are approximately aligned, in this order, so as to minimize the noise due to interplanetary plasma (see Table I and Fig. 13) [18]. The CASSINI radio system has been expressly designed to ensure very high frequency stability. Commands and telecommunications are handled with a two-way link in $X$ band (7.2–8.4 GHz), while precision Doppler experiments exploit a dedicated two-way link at the $K_a$ band (32–34 GHz). The higher carrier frequency reduces the interplanetary plasma noise at levels smaller than $10^{-15}$ for integration times between $10^3$ and $10^4$ sec about solar oppositions. The ground segment at the $K_a$ band is provided by a new, high performance 34 m an-

TABLE III. Main properties of the four fiducial sources used in the text. The assignment of the initial frequency $f_b$, in the case of equal masses and coalescence at the end of the record, determines the final frequency $f_e$ (for a 40-day run), the chirp mass $\mathcal{M}$, and the number of wave cycles, $\mathcal{N}$, recorded at the instrument while the signal sweeps the frequency interval $(f_b,f_e)$.

| $f_b$/Hz | $f_e$/Hz | $\mathcal{M}/M_\odot$ | $\mathcal{N}$ |
|---|---|---|---|
| $10^{-5}$ | $5.3\times10^{-5}$ | $3.6\times10^{7}$ | 52 |
| $5\times10^{-5}$ | $6.9\times10^{-4}$ | $2.9\times10^{6}$ | 273 |
| $10^{-4}$ | $2.1\times10^{-3}$ | $9.2\times10^{5}$ | 550 |
| $5\times10^{-4}$ | $2.7\times10^{-2}$ | $7.1\times10^{4}$ | 2761 |

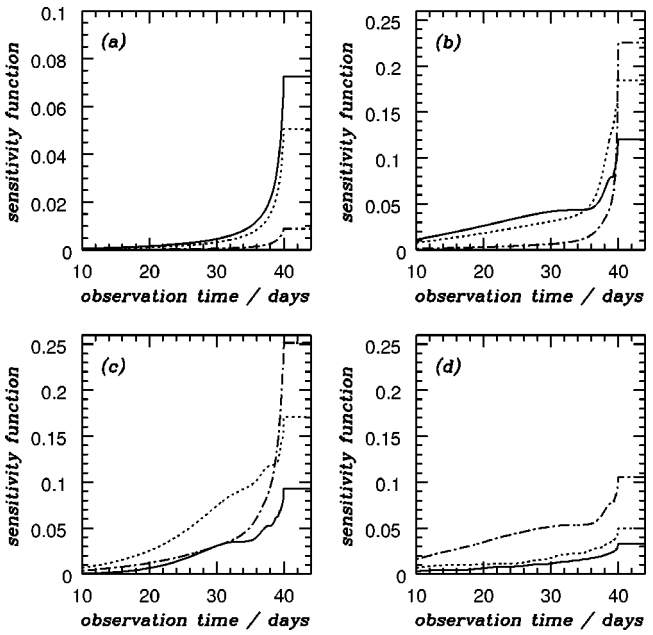


FIG. 10. The behavior of the sensitivity function $\Upsilon$ as a function of $T_1$, for the four fiducial sources described in the text and in Table III [panels (a)–(d), respectively], with $f_b=10^{-5}$, $5\times10^{-5}$, $10^{-4}$, $5\times10^{-4}$ Hz, equal masses, coalescence at the end of the record, and chirp mass almost equal to its the critical value for a 40-day run. The deterioration as $T_1$ decreases reflects the loss of signal-to-noise ratio due to the narrowing of the bandwidth (solid line, $\cos\theta=0$; dotted line, $\cos\theta=0.4$; dot-dashed line, $\cos\theta=0.8$). Notice the different scale in panel (a).

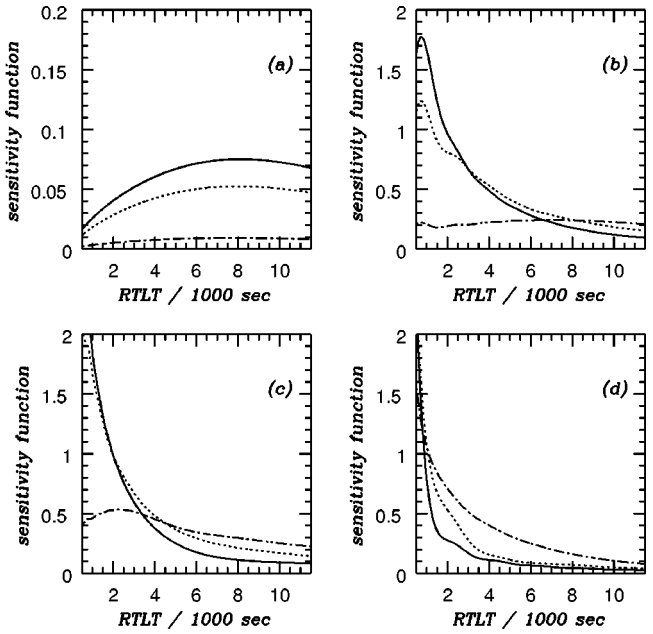


FIG. 11. The behavior of the sensitivity function $\Upsilon$ as a function of the round-trip light time for the same four fiducial sources of the previous figure (solid line, $\cos\theta=0$; dotted line, $\cos\theta=0.4$; dot-dashed line, $\cos\theta=0.8$). Notice the different scale in panel (a).

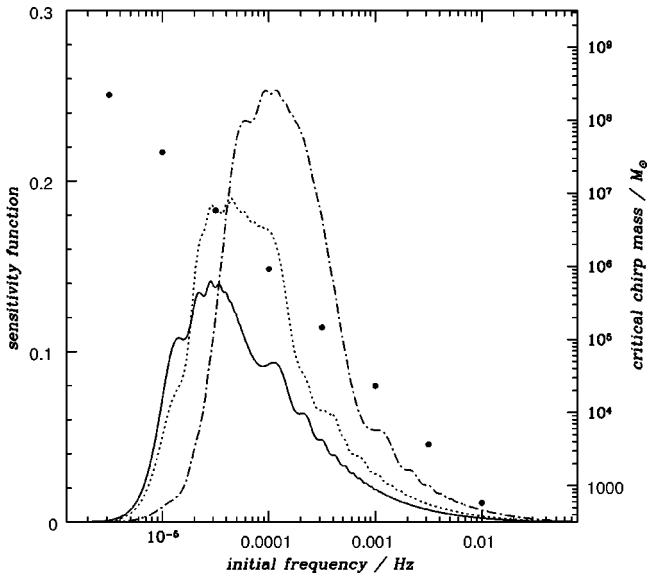


FIG. 12. The behavior of the sensitivity function as a function of the initial frequency $f_b$ for wideband searches of class III, with $f_b = f_B$, $f_e = f_{\rm isco}$, and $T_1 = 40$ days. The corresponding value of the chirp mass—near to the critical value (4.20)—is given by the solid circles (solid line, $\cos\theta = 0$; dotted line, $\cos\theta = 0.4$; dot-dashed line, $\cos\theta = 0.8$).

tenna located in the Goldstone site (California) of NASA's Deep Space Network. Another advanced station will be built in Sardinia (the Sardinia Radio Telescope) and it is hoped that it will track CASSINI in the $K_a$ band (up and down). The radio system of the CASSINI mission has a specification for the overall Allan deviation in the $K_a$ band of $3\times10^{-15}$, for integration times between $10^3$ and $10^4$ sec, one to two

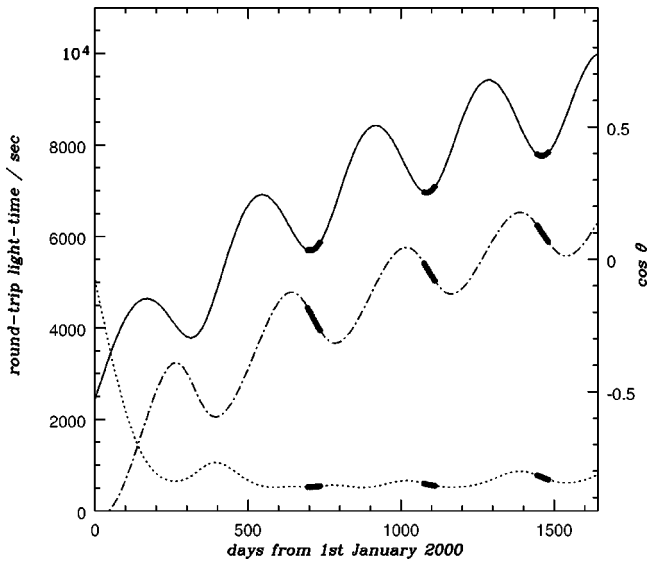


FIG. 13. CASSINI's cruise to Saturn. The solid line gives the round-trip light time $T$ as function of time and we show also the variation of $\cos\theta$ for the Virgo cluster (dash-dotted line) and the galactic center (dotted line). The three gravitational wave experiments (bold lines) take place during days 695–735, 1071–1111, and 1443–1483 from 1 January 2000.

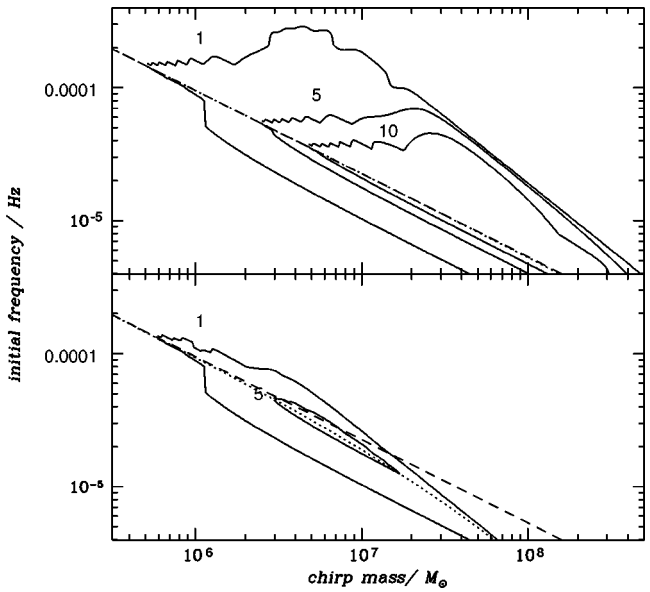


FIG. 14. Detectable inspiral signals emitted by binary systems in the Virgo cluster for the third CASSINI experiment of 40 days. The contour plots of the SNR (in amplitude) for the levels 1, 5, and 10 are shown. The top and bottom panels refer to the mass ratios $M_2/M_1 = 1$ and 0.01, respectively. In the latter case no signals are observable at $\rho \gtrsim 10$. The dashed diagonal line gives the critical chirp mass $\mathcal{M}_c$; see Eq. (4.20). The dotted line marks the transition between signals of class III and IV. Notice that for $M_1 = M_2$ (upper panel) the two lines almost coincide.

orders of magnitude better than previous experiments. In addition, the sensitivity will be improved, with respect to past missions, by the longer time of observation and, possibly, by the combination of the three records. Figure 13 shows the round-trip light time and the value of $\cos\theta$ for the Virgo cluster and the galactic center during the cruise of the space probe to Saturn. Since it turns out that the three planned experiments have comparable sensitivities, we give explicit results only for the last one, in 2004.

Figure 14 shows for the Virgo cluster three different levels of SNR in the plane $(\mathcal{M}, f_b)$: $\rho = 1,\ 5,$ and 10. It confirms the theoretical suggestion that the detectable events of class III lie in a narrow strip below the critical value of the chirp mass. All events above it are of class IV and include the merger. This plot shows how the SNR changes as function of both $\mathcal{M}$ and $f_b$: at $\rho = 1$ and for black holes of comparable masses, the smallest detectable chirp mass is $\simeq 5\times10^5\ M_\odot$. Lower masses are excluded because the systems are too far from coalescence; masses larger than $\sim 10^9\, M_\odot$ are not accessible because their emission frequencies are too low. Note the drastic curtailment if a low frequency cutoff at $1/T \sim 10^{-4}$ Hz is assumed, as was done in the past with ULYSSES; the strongest signals fall below $f_b T = 1$. The SNR is very much reduced when a small mass ratio is assumed (lower panel); an important and unknown factor in assessing the detectability of gravitational radiation from MBHB's is the statistics of this ratio.

One wonders if a source in the Virgo cluster detected in the last opposition is traceable also in the second or the first (albeit at a smaller SNR), thus adding important phase infor-

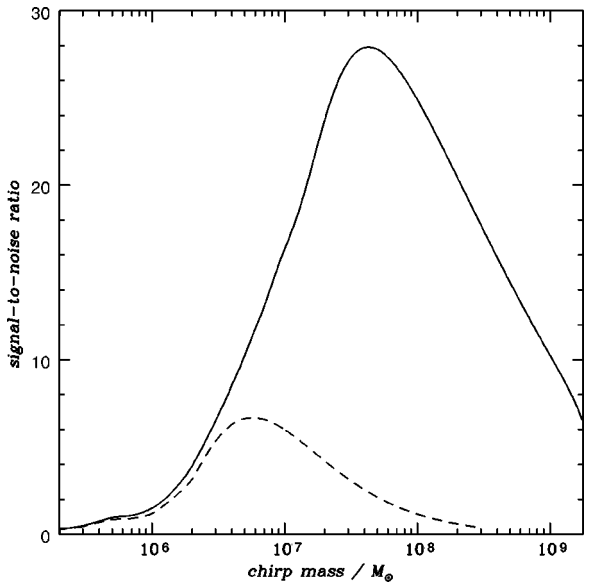


FIG. 15. Signal-to-noise ratio for inspiral signals emitted by binaries in the Virgo cluster ($D=17$ Mpc) with coalescence at the end of the record—that is $f_b=f_B$ and $f_e=f_{\rm isco}$—as a function of the chirp mass. The solid line refers to the case $M_1=M_2$, while the dashed line to $M_2/M_1=0.01$. We have considered the CASSINI third opposition and $T_1=40$ days.

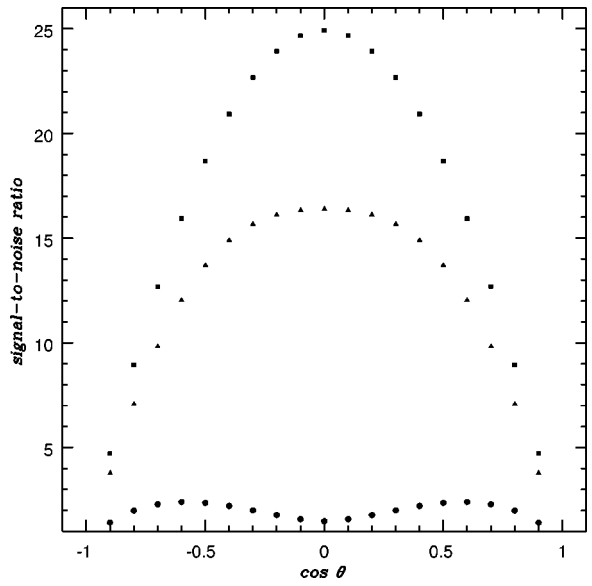


FIG. 16. The signal-to-noise ratio as a function of cos $\theta$ during the CASSINI third opposition, $T_1=40$ days, for inspiral signals emitted by binary systems located at the same distance of the Virgo cluster ($D=17$ Mpc) with $f_b=f_B$ and $f_e=f_{\rm isco}$, that is final coalescence at the end of the record (squares, $\mathcal{M}=10^8\,M_\odot$; triangles, $M_\odot=10^7\,M_\odot$; circles, $M_\odot=10^6\,M_\odot$; for all $\eta=1/4$). The decrease for $|\cos\theta|\to 1$ is, of course, due to the approach to the case of propagation along the instrument's beam; the saddle in correspondence of $|\cos\theta|\simeq 0$ for $\mathcal{M}=10^6\,M_\odot$ is due to the fact that the frequency band swept by the signal encounters a minimum of the response function at $fT\approx 1$, which vanishes for $\cos\theta=0$ (see Figs. 4 and 7).

mation. We checked that for $T_1=40$ days this is not the case: detectable sources are too near coalescence, in relation to the (roughly) 1 yr separation between different runs. We have then tried doubling the observation time to $T_1=80$ days (''extended'' experiments) and interestingly found that for some sources the three extended data sets can be combined: the strongest sources detectable in one opposition are also visible in the previous one. A single, extended experiment does not show drastic improvements over the nominal record; however, the accessible portion of the plane $(\mathcal{M},f_b)$ becomes slightly wider. Of course, a drastic improvement in sensitivity and detection probability would be expected for a continuous run of a few years.

How far is the farthest detectable system? From Fig. 15 we see that the highest SNR, about 28, produced by a source in the Virgo cluster is attained for a system of comparable masses $\simeq 5\times 10^7\,M_\odot$; at $\rho=1$ this corresponds to a distance $\approx 600$ Mpc; if $M_2/M_1=10^{-2}$, the ken is reduced by a factor $\simeq 5$.

In order to have an idea of the change in SNR due to different angles $\theta$, in Fig. 16 we have studied this dependence for the third experiment in three different cases: $\mathcal{M}=10^6 M_\odot$, $10^7 M_\odot$, $10^8 M_\odot$ ($f_b=f_B$, $f_e=f_{\rm isco}$, $\eta=1/4$). Note that, for $\mathcal{M}=10^6\,M_\odot$, $\cos\theta=0$ is a local minimum, rather than the expected maximum: this is due to the fact that signals fall in one of the high frequency minima of the three-pulse response; see Figs. 4 and 7. Figures 14, 15, and 16 therefore allow one to have an overall picture of the all-sky sensitivity of CASSINI; see Eqs. (4.16) and (4.17).

We turn now to galactic observations and consider a binary system in the center of our galaxy composed of a primary black hole of mass $M_1=2\times 10^6\,M_\odot$, whose existence is strongly inferred from observations carried out over the past 25 years [55], and a secondary, smaller object of mass $M_2$. In Fig. 17 we show for the third CASSINI opposition the SNR contour levels $\rho=1,5,100$ in the plane $(M_2,f_b)$. Of course, there is no signal above

$$f_{\rm isco}\simeq 2\times 10^{-3}\left(\frac{M_1}{2\times 10^6\,M_\odot}\right)^{-1}\ {\rm Hz}$$

[cf. Eq. (2.13)], essentially independent of $M_2$. CASSINI proves to be a fairly sensitive instrument for such signals; in fact, each of the three experiments is sensitive to secondary objects of mass down to $\sim 10M_\odot$–$50M_\odot$ and for $M_2 \gtrsim 100\,M_\odot$ the expected SNR can be $\gg 10$; see Fig. 18. Remarkably, most of the sources visible during one experiment are detectable also in the others; in fact the time to coalescence is $\simeq 2995\,(f_b/5\times 10^{-4}\ {\rm Hz})^{-8/3}(100\,M_\odot/\mu)(2\times 10^6\,M_\odot/M)^{2/3}$ days (cf. also Fig. 19). If a candidate signal is spotted in one of the data sets, it is therefore possible to chase it also in the other oppositions, which provides a robust method of accepting or discarding detection by coherently tracking the gravitational phase over a period of some years. This is a direct consequence of the fact that many signals would be recorded as class II and III (therefore far from the final coalescence) as is shown in Fig. 17 by the dotted and dashed lines in the plane $(M_2,f_b)$; this is in contrast with what appends for observations in the Virgo cluster, where most of the signals show up as class IV. The good

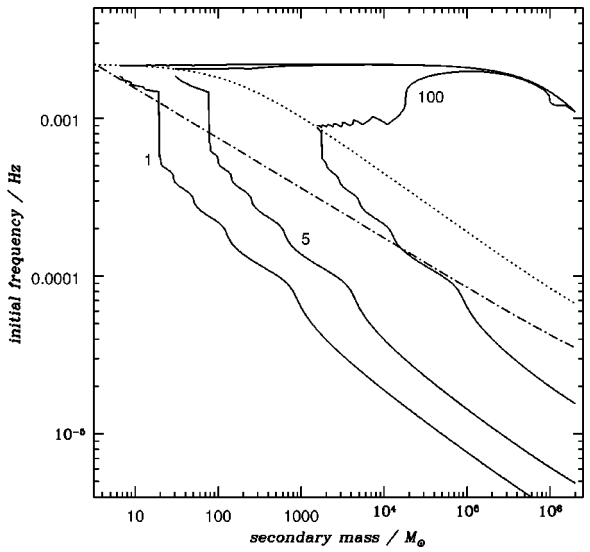


FIG. 17. Detectability of radiation emitted by the inspiral of a secondary black hole of mass $M_2$ orbiting a primary object with mass $M_1=2\times10^6\,M_\odot$, in the galactic center ($D\simeq8$ kpc) during the CASSINI third experiment ($T_1=40$ days). The contour plots of SNR $=1$, 5, and 100 in the plane $(M_2,f_b)$ are shown. The dash-dotted line divides the plane $(M_2,f_b)$ in signal of class II (below) and III (above), while above the dotted line the signals are registered as of class IV.

sensitivity for nearby sources also allows one to search for possible binary systems in other galaxies of the Local Group.

It is interesting to compare CASSINI's sensitivity with past Doppler experiments (Table I). The best Doppler data available today come from observations carried out in 1991,

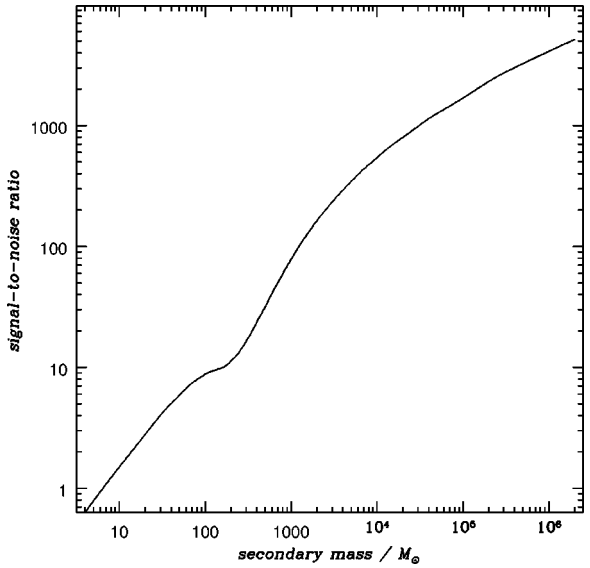


FIG. 18. Expected optimal signal-to-noise ratio produced in CASSINI records by inspiraling binaries in the galactic center. The plot shows the maximum SNR—i.e., computed for $f_b=f_B$ and coalescence at the end of the record ($T_1=40$ days), and therefore $f_e=f_{\rm isco}$—produced by binary systems with $M_1=2\times10^6\,M_\odot$ and a secondary black hole of mass $M_2\leqslant M_1$ as a function of $M_2$, during the CASSINI third opposition.

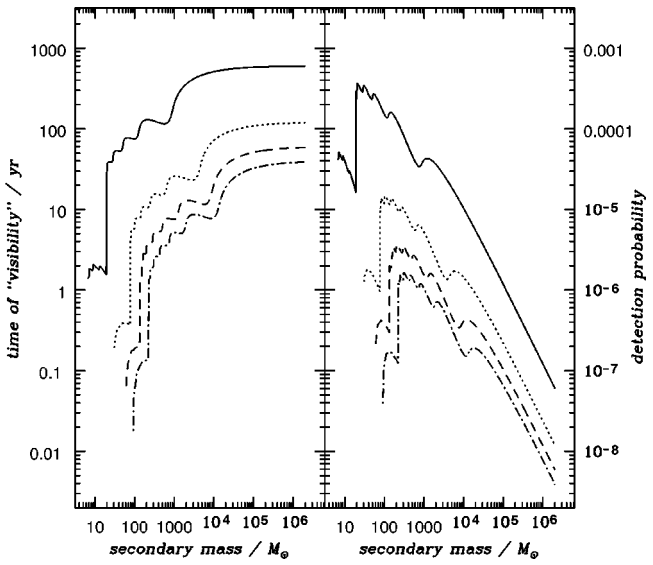


FIG. 19. Time of ''visibility'' $T_D$ and probability of success for the detection of radiation emitted by the inspiral of a secondary black hole into a primary of mass $M_1=2\times10^6\,M_\odot$ in our galactic center during the CASSINI third opposition. The curves refer to four different thresholds of detection ($\rho_{\rm D}=1$, solid line; $\rho_{\rm D}=5$, dotted line; $\rho_{\rm D}=10$, dashed line; $\rho_{\rm D}=15$, dot-dashed line).

1992, and 1993 with the probes ULYSSES, GALILEO, and Mars Observer. In 1993 all three spacecraft have been simultaneously tracked for about 3 weeks, with a triple coincidence experiment whose data are being analyzed; this experiment will be useful to search for signals coming from the merger phase [16].

We concentrate on the ULYSSES 1992 experiment [14,15]. After preprocessing, only 14 days of data have been retained, around the Sun opposition. Their Allan deviation (at 1000 sec) is variable, with only its best value near the specification, $3\times10^{-14}$. Data outside the bandwidth $\simeq2.3\times10^{-4}-5\times10^{-2}$ Hz have been discarded (see Fig. 5): at high frequencies the data are affected by the rotational dynamics of the spacecraft and by thermal noise; low frequencies were cutoff by high-pass filtering. In the intermediate band the noise spectrum is well approximated by a power law $\propto f^{-0.5}$ (see Table II). The low frequency cutoff limits, for events of class III, the chirp mass to values below the critical chirp mass [Eq. (4.20)]

$$\mathcal{M}_c=5\times10^5\left(\frac{f_b}{2.3\times10^{-4}\ \text{Hz}}\right)^{-8/5}\left(\frac{T_1}{14\,\text{days}}\right)^{-3/5}M_\odot\,. \tag{4.27}$$

Equation (4.27) clearly indicates that the most interesting region in the $(\mathcal{M},f_b)$ plane is not accessible (cf. Fig. 14) and therefore the largest attainable distance is strongly reduced. Moreover, the noise spectral density, as defined by Eqs. (4.12)–(4.15) with the parameters reported in Table II (see Fig. 5), is about two orders of magnitude larger than for CASSINI. According to Eq. (4.10), the ideal *ken* (we recall that it is defined for SNR $=1$) is

$$D_{\rm id}\simeq 1\left(\frac{\mathcal{M}}{1.3\times 10^5 M_\odot}\right)^{5/6}\left(\frac{S_0}{2.5\times 10^{-24}\ \ {\rm Hz}^{-1}}\right)^{-1/2}\times\left(\frac{T}{4430\,{\rm sec}}\right)^{2/3}{\rm Mpc}. \tag{4.28}$$

Therefore, in conventional astrophysical scenarios, ULYSSES experiments are relevant only for the galactic center (whose angular position with respect to the spacecraft was $\theta\approx 109°$) and the Local Group. It is straightforward to check that at $\rho=5$ secondary black holes with $M_2\gtrsim 10^3 M_\odot$ would be detectable.

## V. CONCLUSIONS

We have analyzed the sensitivity of Doppler detectors to gravitational waves emitted by coalescing binaries in their inspiral phase. For CASSINI experiments sources in the Virgo cluster would be observable at a signal-to-noise ratio up to $\simeq 30$; furthermore, binary systems with $M_1\sim M_2\sim 5\times 10^7 M_\odot$ at distance $\sim 600$ Mpc are within the range of the instrument. If in the center of our galaxy there is a massive black hole of $2\times 10^6 M_\odot$, orbiting black holes with mass $\gtrsim 50 M_\odot$ would be easily detectable; for larger masses the signal-to-noise ratio can be considerably higher and therefore one can reach other galaxies within the Local Group. These are considerable improvements in sensitivity and range of accessible masses with respect to past Doppler experiments.

This analysis has been made in relation to astrophysically reasonable sources, but without any concern for the probability of such events and their detection. Considering our ignorance about sources of gravitational waves, in particular for events in galactic nuclei, this point of view appears reasonable, especially for nondedicated experiments like CASSINI; however, it is healthy and sobering to assess what one can predict on the basis of *very simple and conventional astrophysical models*. The estimation of the event rate is a much debated problem in low frequency gravitational wave experiments (see [19,32,35,36,39] and references therein), with sensitivity not good enough to detect signals from known stellar mass galactic binaries. We briefly consider here two models: (a) accretion of small black holes onto a massive one in a galactic core and (b) coalescence of two MBHB's of comparable mass, possibly resulting from the mergers of two galaxies. In the context of Doppler experiments, they are appropriate for small and large distances, respectively.

Let us consider now case (a). Suppose that a central black hole $M$ in a typical galaxy (i.e., in our galactic center) has captured $N=M/M_2$ masses $M_2$ at the uniform rate $R=H_0 M/M_2$ during the whole life of the Universe, $H_0^{-1}\simeq 10^{10} h_{100}$ yr, where $h_{100}$ is the Hubble constant normalized to 100 $\rm km\,sec^{-1}\,Mpc^{-1}$; each of these captures gives rise to a chirp.

In order to determine the probability of success, consider first a given secondary mass $M_2$ (and a fixed primary $M_1$, which determines the chirp mass). The SNR is largest when coalescence occurs at the end of the record, so that the initial frequency is $f_b=f_B$ [Eq. (2.18)]; its value is plotted in Fig. 18 as a function of $M_2$. But we can detect the signal also at a smaller SNR, when $f_b$ is smaller and the source far from coalescence. The SNR decreases essentially because the bandwidth is smaller. For a given minimum $\rho_D$ in the SNR we have computed the ''visibility time'' $T_D$ (which depends on $M_2$) and plotted it in Fig. 19, together with the detection probability $RT_D=T_D(M_2)H_0 M/M_2$, as a function of $M_2$. This probability has a maximum (with large $M_2$ the visibility time increases, but the expected number of events decreases). This determines the most favorable value of $M_2$, about $100M_\odot$, and the corresponding (optimistic) success probability in each experiment, about $10^{-5}$.

We turn now to case (b). To go to very large distances and to reach the largest number of sources, we must aim at large masses and use low frequencies, in the band $fT<1$. In this frequency range, the noise spectral density is well described by a single power law $S_n(f)\simeq S_0(f/f_1)^{\alpha_1}$. Detection of large masses at large distances may conflict with the redness of the noise. To analyze this limitation, consider a wideband-detected signal at low frequency $f_b\approx f_e-f_b\ll 1/T$; then we can use the approximation (3.10) for the response and obtain

$$\rho^2=k\frac{T^{4/3}\mathcal{M}^{5/3}}{S_0 D^2}(Tf_b)^{2/3-\alpha_1}(Tf_1)_1^{\alpha}, \tag{5.1}$$

where $k$ is a dimensionless coefficient. One wonders if greater distances can be reached by decreasing $f_b$. To answer this question, let us concentrate on the dependence on $f_b$:

$$\rho^2\propto\frac{\mathcal{M}^{5/3}}{D^2}f_b^{2/3-\alpha_1}\propto f_b^{-2-\alpha_1}, \tag{5.2}$$

where we have used the approximation $\mathcal{M}\approx\mathcal{M}_c\propto f_b^{-8/5}$ for the chirp mass [see Eq. (4.20)]. For a given SNR the total number of detectable sources with this chirp mass is of order

$$N\propto D^3\propto f_b^{-3(1+\alpha_1/2)} \tag{5.3}$$

and increases with decreasing frequency if $\alpha_1>-2$. The nominal case $\alpha_1=-2$ separates the two alternatives, whether it useful or not to go to lower frequencies.

If we assume (naively and optimistically) that each galaxy in the Universe contains a massive black hole and has undergone $N_{\rm m}$ merging events leading to the formation of a binary with time to coalescence shorter than the Hubble time, we can estimate the event rate as $R=N_{\rm m}N_{\rm g}H_0$, where $N_{\rm g}$ is the total number of detectable galaxies. As we have seen in the previous section, with the nominal noise the *ken* of CASSINI is $D\sim 600$ Mpc and therefore the probability of detection is

$$P\sim 2\times 10^{-3} N_{\rm m}\left(\frac{N_{\rm g}}{10^{10}}\right)\left(\frac{3\,T_1}{120\,{\rm days}}\right)\left(\frac{D}{600\,{\rm Mpc}}\right)^3\left(\frac{H_0}{3\,{\rm Gpc}}\right)^4. \tag{5.4}$$

Of course, larger distances could be attained if we knew the waveform produced during the final collapse and the merger could be included in the search. In the present situation of ignorance, however, a good level of confidence in the detection of merger signals requires coincidence experiments.

We conclude that, in conventional astrophysical scenarios, the events we are looking for do not have a large probability to be detected, the extragalactic case (b) being more favorable.

Present Doppler experiments are relatively cheap, but use nondedicated spacecraft and are limited in instrumentation, orbits, observation time and by several other constraints. However, despite their low sensitivity, they are the only one that at present can access the coalescence of binaries involving massive objects, and therefore quite valuable. They might discover gravitational waves; if they do not, they will provide interesting astrophysical limits on massive sources, in particular in our galactic center, the Local Group, and the Virgo cluster. Since real data are already available in large amounts and the search techniques are very similar to those implemented for Earth-based (and, in future, space-borne) laser interferometers, Doppler experiments can also be used to test filtering and processing techniques.

## ACKNOWLEDGMENTS

We are very grateful to J. W. Armstrong for his continuous collaboration in Doppler experiments and his comments. We also thank H. D. Wahlquist and F. B. Estabrook for extensive discussions and C. Cutler for very helpful comments and advice regarding Sec. II B. B.B. and L.I. would like to thank the Agenzia Spaziale Italiana for financial support. A.V. acknowledges the kind hospitality of Cardiff University during the early stage of this work and the Carlo A. Sacchi Foundation for financial support. L.I. would like to thank the Jet Propulsion Laboratory, California Institute of Technology, where part of this work was performed and NRC-NASA for financial support.

[1] A. Abramovici *et al.*, Science **256**, 325 (1992).
[2] C. Bradaschia *et al.*, Nucl. Instrum. Methods Phys. Res. A **289**, 518 (1990).
[3] K. Danzmann, in *Gravitational Wave Experiments*, edited by E. Coccia, G. Pizzella, and F. Ronga (World Scientific, Singapore, 1995), pp. 100–111.
[4] K. Tsubono, in *Gravitational Wave Experiments*, edited by E. Coccia, G. Pizzella, and F. Ronga (World Scientific, Singapore, 1995), pp. 112–114.
[5] P. Astone *et al.*, Phys. Lett. B **385**, 421 (1996).
[6] P. Astone *et al.*, Astropart. Phys. **7**, 231 (1997).
[7] M. Cerdonio *et al.*, in *Gravitational Wave Experiments* [4], pp. 176–194.
[8] E. Mauceli, Z. K. Geng, W. O. Hamilton, W. W. Johnson, S. Merkowitz, A. Morse, B. Price, and N. Solomonson, Phys. Rev. D **54**, 1264 (1996).
[9] D. Blair *et al.*, in *Gravitational Wave Experiments* [4], pp. 144–160.
[10] F. B. Estabrook and H. R. Wahlquist, Gen. Relativ. Gravit. **6**, 439 (1975).
[11] R. W. Hellings, P. S. Callahan, and J. D. Anderson, Phys. Rev. D **23**, 844 (1991).
[12] J. D. Anderson *et al.*, Nature (London) **308**, 158 (1984).
[13] J. W. Armstrong, F. B. Estabrook, and H. D. Wahlquist, Astrophys. J. **318**, 536 (1987).
[14] B. Bertotti *et al.*, Astron. Astrophys., Suppl. Ser. **92**, 431 (1992).
[15] B. Bertotti, R. Ambrosini, J. Armstrong, S. W. Asmar, G. Comoretto, G. Giampieri, Y. Koyama, L. Iess, A. Messeri, A. Vecchio, and H. D. Wahlquist, Astron. Astrophys. **296**, 13 (1995).
[16] J. W. Armstrong, in *Second Amaldi Conference on Gravitational Waves*, edited by E. Coccia *et al.* (World Scientific, Singapore, in press); L. Iess, J. W. Armstrong, B. Bertotti, H. D. Wahlquist, and F. B. Estabrook, presented at the 15th International Conference of General Relativity and Gravitation, Pune, 1997.
[17] CASSINI mission: references and information on WWW at http://www.jpl.nasa.gov/cassini.
[18] G. Comoretto, B. Bertotti, L. Iess, and R. Ambrosini, Nuovo Cimento C **15**, 1193 (1992).
[19] P. Bender *et al.*, ''LISA Pre-Phase A Report,'' 2nd ed., Report No. MPQ 233, 1998.
[20] R. W. Hellings, ''Ω Orbiting Medium Explorer for Gravitational Astrophysics,'' mixed proposal, 1995.
[21] B. Bertotti, in *Proceedings of the 14th International Conference on General Relativistic Gravity*, edited by M. Francaviglia *et al.* (World Scientific, Singapore, 1997), p. 79.
[22] K. S. Thorne, in *Proceedings of the Snowmass 95 Summer Study on Particle and Nuclear Astrophysics and Cosmology*, edited by E. W. Kolb and R. Peccei (World Scientific, Singapore, 1995), p. 398.
[23] K. S. Thorne, in *Black Holes and Relativistic Stars*, edited by R. Wald (University of Chicago Press, Chicago, 1998), pp. 41–77.
[24] K. S. Thorne and V. B. Braginsky, Astrophys. J., Lett. Ed. **204**, L1 (1976).
[25] V. M. Lipunov and K. A. Postnov, Sov. Astron. **31**, 228 (1987).
[26] V. M. Lipunov, K. A. Postnov, and M. E. Prokhorov, Sov. Astron. **31**, 228 (1987).
[27] D. Hils, P. L. Bender, and R. F. Webbink, Astrophys. J. **360**, 75 (1990).
[28] R. A. Hulse, Rev. Mod. Phys. **66**, 699 (1994).
[29] J. H. Taylor, Rev. Mod. Phys. **66**, 711 (1994).
[30] J. H. Taylor and J. M. Weisberg, Astrophys. J. **345**, 434 (1989).
[31] D. Hils and P. L. Bender, Astrophys. J. Lett. **445**, L7 (1995).
[32] S. Sigurdsson and M. J. Rees, Mon. Not. R. Astron. Soc. **284**, 318 (1996).

[33] M. Shibata, Phys. Rev. D **50**, 6297 (1994).
[34] M. C. Begelman, R. D. Blandford, and M. J. Rees, Nature (London) **287**, 307 (1980).
[35] M. G. Haehnelt, Mon. Not. R. Astron. Soc. **269**, 199 (1994).
[36] A. Vecchio, Class. Quantum Grav. **14**, 1431 (1997).
[37] R. R. Caldwell and B. Allen, Phys. Rev. D **45**, 3447 (1992).
[38] G. Giampieri and A. Vecchio, Gen. Relativ. Gravit. **27**, 793 (1995).
[39] P. L. Bender and D. Hils, Class. Quantum Grav. **14**, 1439 (1997).
[40] K. A. Postnov and M. E. Prokhorov, Astrophys. J. **494**, 674 (1998).
[41] D. I. Kosenko and K. A. Postnov, ''On the gravitational wave noise from unresolved extragalactic binaries,'' astro-ph/9801032.
[42] M. J. Rees, Proc. Natl. Acad. Sci. USA **90**, 4840 (1993).
[43] M. Haehnelt and M. J. Rees, Mon. Not. R. Astron. Soc. **263**, 168 (1993).
[44] A. Loeb and F. A. Rasio, Astrophys. J. **432**, 52 (1994).
[45] Y. B. Zel'dovich and I. D. Novikov, Sov. Phys. Dokl. **158**, 811 (1964).
[46] E. E. Salpeter, Astrophys. J. **140**, 796 (1964).
[47] R. D. Blandford, in *Active Galactic Nuclei*, edited by T. Courvoisier and M. Mayor (Springer-Verlag, Berlin, 1990).
[48] D. E. Osterbrock, Astrophys. J. **404**, 551 (1993).
[49] M. J. Rees, Science **247**, 817 (1990).
[50] J. Kormendy and D. Richstone, Annu. Rev. Astron. Astrophys. **33**, 581 (1995).
[51] S. Tremaine, in *Some Unsolved Problems in Astrophysics*, edited by J. Bahcall and J. P. Ostriker (Princeton University Press, Princeton, 1996).
[52] R. P. van der Marel, in *New Light on Galaxy Evolution*, edited by R. Bender and R. L. Davies (Kluwer, Dordrecht, 1996), pp. 117–120.
[53] M. J. Rees, in *Black Holes and Relativistic Stars*, edited by R. Wald (University of Chicago Press, Chicago, 1998), p. 79–101.
[54] M. Miyoshi, J. Moran, J. Herrnstein, L. Greenhill, N. Nakai, P. Diamond, and M. Inoue, Nature (London) **373**, 127 (1995).
[55] A. Eckart and R. Genzel, Nature (London) **383**, 415 (1996).
[56] E. Maoz, Astrophys. J. Lett. **447**, L91 (1995).
[57] E. Maoz, Astrophys. J. Lett. **494**, L181 (1998).
[58] J. E. Barnes and L. Hernquist, Annu. Rev. Astron. Astrophys. **30**, 705 (1992).
[59] U. Fritze–von Alvensleben, in *From Stars to Galaxies: The Impact of Stellar Physics on Galaxy Evolution*, edited by C. Leitherer, U. Fritze–von Alvensleben, and J. Huchra, ASP Conference Series 98 (1996), p. 496.
[60] N. Roos, Astron. Astrophys. **104**, 218 (1981).
[61] C. M. Gaskell, in *Jets from Stars and Galaxies*, edited by W. Kundt (Springer, Berlin, 1996), pp. 165–196.
[62] N. Roos, J. S. Kastra, and C. A. Hummel, Astrophys. J. **409**, 130 (1993).
[63] A. Sillanpää, S. Haarala, M. J. Valtonen, B. Sundelius, and G. G. Byrd, Astrophys. J. **325**, 628 (1988).
[64] L. Valtoja, M. J. Valtonen, and G. G. Byrd, Astrophys. J. **343**, 47 (1989).
[65] C. M. Gaskell, Astrophys. J. **646**, L107 (1996).
[66] E. Poisson, Phys. Rev. D **54**, 5939 (1996).
[67] F. D. Ryan, Phys. Rev. D **56**, 1845 (1997).
[68] P. C. Peters, Phys. Rev. **136**, B1224 (1964).
[69] S. Mikkola and M. J. Valtonen, Mon. Not. R. Astron. Soc. **259**, 115 (1992).
[70] A. G. Polnarev and M. J. Rees, Astron. Astrophys. **283**, 301 (1994).
[71] A. Vecchio, M. Colpi, and A. G. Polnarev, Astrophys. J. **433**, 733 (1994).
[72] H. D. Wahlquist, Gen. Relativ. Gravit. **19**, 1101 (1887).
[73] B. F. Schutz, in *The Detection of Gravitational Waves*, edited by D. Blair (Cambridge University Press, Cambridge, England, 1989), pp. 406–427.
[74] B. F. Schutz, in Proceedings of the 1997 Alpbach Summer School on Fundamental Physics in Space, edited by A. Wilson (ESA, 1997), Report No. AEI-044.
[75] S. Smith, Phys. Rev. D **36**, 2901 (1987).
[76] J. D. Anderson, F. B. Estabrook, and H. D. Wahlquist, Astrophys. J. **318**, 536 (1987).
[77] M. Tinto and J. W. Armstrong, Astrophys. J. **372**, 545 (1991).
[78] B. F. Schutz, Nature (London) **323**, 310 (1986).
[79] M. Tinto, Phys. Rev. D **53**, 5354 (1996).
[80] In order to extract the signal in a reliable and accurate way, the wave phase needs to be modeled including post-Newtonian correction terms [81,82]. The phase evolution is currently known, in the finite mass case, up to the post$^{2.5}$-Newtonian order [83–87]. The post$^{3}$-Newtonian terms seem also to be under control now [88,89].
[81] C. M. Will, in *Relativistic Cosmology*, edited by M. Sasaki (Universal Academy Press, Japan, 1994), p. 83.
[82] L. Blanchet, presented at the ''Les Houches School on Gravitational Radiation,'' gr-qc/9607025.
[83] L. Blanchet, T. Damour, B. R. Iyer, C. M. Will, and A. G. Wiseman, Phys. Rev. Lett. **74**, 3515 (1995).
[84] L. Blanchet, T. Damour, and B. R. Iyer, Phys. Rev. D **51**, 5360 (1995).
[85] C. M. Will and A. G. Wiseman, Phys. Rev. D **54**, 4813 (1996).
[86] L. Blanchet, B. R. Iyer, C. M. Will, and A. G. Wiseman, Class. Quantum Grav. **13**, 575 (1996).
[87] L. Blanchet, Phys. Rev. D **54**, 1417 (1996).
[88] L. Blanchet, Class. Quantum Grav. **15**, 1971 (1998).
[89] L. Blanchet, B.R. Iyer, and B. Joguet (unpublished).
[90] C.W. Misner, K. S. Thorne, and J. A. Wheeler, *Gravitation* (Freeman, New York, 1973).
[91] The angles $\varphi$ and $\iota$ can be regarded as constant only in the limit of negligible spins; otherwise the coupling of the black hole spins with the binary orbital angular momentum (the so-called *spin-orbit* and *spin-spin couplings*) causes the orbital plane to precess, which induces amplitude and phase modulations [92,93]. In the lowest-order Newtonian quadrupole approximation, which we are considering here, these effects do not appear and, accordingly, we will ignore them.
[92] T. A. Apostolatos, C. Cutler, G. S. Sussman, and K. S. Thorne, Phys. Rev. D **49**, 6274 (1994).
[93] L. E. Kidder, Phys. Rev. D **52**, 821 (1995).
[94] E. Seidel, in ''Numerical Relativity: Towards Simulations of 3D Black Hole Coalescence,'' in *Gravitation and Relativity: At the Turn of the Millennium*, edited by N. Dadhich and J.

Narlikar (IUCAA, Pune, 1998), pp. 107–137.
[95] Numerical Relativity Grand Challenge Alliance, 1995. References and information on WWW at http://jean-luc.ncsa.uiuc.edu/GC.
[96] J. Pullin, in *Gravitation and Relativity: At the Turn of the Millennium* [94], pp. 87–105.
[97] J. K. Blackburn and S. Detweiler, Phys. Rev. D **46**, 2318 (1992).
[98] L. E. Kidder, C. M. Will, and A. G. Wiseman, Phys. Rev. D **47**, 3281 (1993).
[99] L. E. Kidder, C. M. Will, and A. G. Wiseman, Class. Quantum Grav. **9**, L125 (1993).
[100] G. B. Cook, Phys. Rev. D **50**, 5025 (1994).
[101] The inequalities in Eqs. (2.19)–(2.21) are slightly pessimistic because they consider the total frequency change from the beginning frequency, while one could consider the frequency change from the middle frequency and obtain a value about 2 times smaller, as we have done in [15].
[102] C. Cutler and E. E. Flanagan, Phys. Rev. D **49**, 2658 (1994).
[103] E. Flanagan and S. Hughes, Phys. Rev. D **57**, 4535 (1998).
[104] L. L. Smarr, in *Sources of Gravitational Radiation*, edited by L. L. Smarr (Cambridge University Press, Cambridge, England, 1979).
[105] The Allan variance $\sigma_y(\tau)$ of a random process $y(t)$ for a time of integration $\tau$ is defined as $\sigma_y^2(\tau)=\langle[Y(t)-Y(t+\tau)]^2/2\rangle$, where $Y(t)=\int_t^{t+\tau} y(x)\,dx$ and $\langle\ \rangle$ stands for ansamble average. See, e.g., J. W. Armstrong, in *Gravitational Wave Data Analysis*, edited by B. F. Schutz (Kluwer, Dordrecht, 1989), p. 153.
[106] J. A. Barnes *et al.*, IEEE Trans Instrum. Meas. **IM-20**, 105 (1971).
[107] T. Damour, B. R. Iyer, and B. S. Sathyaprakash, Phys. Rev. D **57**, 885 (1998).